

REPORT DOCUMENTATION PAGE				Form Approved OMB NO. 0704-0188	
<p>The public reporting burden for this collection of information is estimated to average 1 hour per response, including the time for reviewing instructions, searching existing data sources, gathering and maintaining the data needed, and completing and reviewing the collection of information. Send comments regarding this burden estimate or any other aspect of this collection of information, including suggestions for reducing this burden, to Washington Headquarters Services, Directorate for Information Operations and Reports, 1215 Jefferson Davis Highway, Suite 1204, Arlington VA, 22202-4302. Respondents should be aware that notwithstanding any other provision of law, no person shall be subject to any penalty for failing to comply with a collection of information if it does not display a currently valid OMB control number.</p> <p>PLEASE DO NOT RETURN YOUR FORM TO THE ABOVE ADDRESS.</p>					
1. REPORT DATE (DD-MM-YYYY) 24-04-2012		2. REPORT TYPE Final Report		3. DATES COVERED (From - To) 16-Sep-2009 - 16-Sep-2011	
4. TITLE AND SUBTITLE A Multiscale Software Tool for Field/Circuit Simulation Final Report				5a. CONTRACT NUMBER	
				5b. GRANT NUMBER W911NF-09-C-0159	
				5c. PROGRAM ELEMENT NUMBER 665502	
6. AUTHORS Junhuo Lee, Mengqing Yuan, Qing Huo Liu				5d. PROJECT NUMBER	
				5e. TASK NUMBER	
				5f. WORK UNIT NUMBER	
7. PERFORMING ORGANIZATION NAMES AND ADDRESSES Wave Computation Technologies, Inc. 1800 Martin Luther King Jr. Parkway Suite 204 Durham, NC 27707 -3500				8. PERFORMING ORGANIZATION REPORT NUMBER	
9. SPONSORING/MONITORING AGENCY NAME(S) AND ADDRESS(ES) U.S. Army Research Office P.O. Box 12211 Research Triangle Park, NC 27709-2211				10. SPONSOR/MONITOR'S ACRONYM(S) ARO	
				11. SPONSOR/MONITOR'S REPORT NUMBER(S) 55217-EL-ST2.8	
12. DISTRIBUTION AVAILABILITY STATEMENT Approved for Public Release; Distribution Unlimited					
13. SUPPLEMENTARY NOTES The views, opinions and/or findings contained in this report are those of the author(s) and should not be construed as an official Department of the Army position, policy or decision, unless so designated by other documentation.					
14. ABSTRACT This report is developed under topic #A08-T004, contract W911NF-09-C-0159. As the final report, we have developed a new multiscale field/circuit solver by combining three efficient methods including the SETD method, FETD method, ECT method, and circuit solver. We have designed simple multidomain structure to support several different methods and their coupling required by the multiscale hybrid algorithm. Based on the architecture we have completed the development of the hybrid SETD/FETD/ECT/ Circuit engine for multiscale simulation.					
15. SUBJECT TERMS STTR Report, Multidomain Hybrid Method, Spectral-Element Time-Domain method, Finite-Element Time-Domain method,					
16. SECURITY CLASSIFICATION OF:			17. LIMITATION OF ABSTRACT UU	15. NUMBER OF PAGES	19a. NAME OF RESPONSIBLE PERSON Tian Xiao
a. REPORT UU	b. ABSTRACT UU	c. THIS PAGE UU			19b. TELEPHONE NUMBER 919-419-1500

Report Title

A Multiscale Software Tool for Field/Circuit Simulation

Final Report

ABSTRACT

This report is developed under topic #A08-T004, contract W911NF-09-C-0159. As the final report, we have developed a new multiscale field/circuit solver by combining three efficient methods including the SETD method, FETD method, ECT method, and circuit solver. We have designed simple multidomain structure to support several different methods and their coupling required by the multiscale hybrid algorithm. Based on the architecture we have completed the development of the hybrid SETD/FETD/ECT/ Circuit engine for multiscale simulation. Furthermore to increase efficiency we have completed the parallel computation for our hybrid method based on multi-scale field/circuit package. And we also have completed the implementation of hardware (GPU) acceleration method for the package. To verify our package, we have completed comprehensive tests of the field/circuit package.

Enter List of papers submitted or published that acknowledge ARO support from the start of the project to the date of this printing. List the papers, including journal references, in the following categories:

(a) Papers published in peer-reviewed journals (N/A for none)

<u>Received</u>	<u>Paper</u>
2012/04/24 0' 2	Lin Wang, Meng Qing Yuan, Qing Huo Liu. A Dual-Band Printed Electrically Small Antenna Covered by Two Capacitive Split-Ring Resonators, IEEE Antennas and Wireless Propagation Letters, (08 2011): 824. doi: 10.1109/LAWP.2011.2164890
2012/04/24 0' 1	Lin Wang, Tian Xiao, W. T. Joines, Mengqing Yuan, Q. H. Liu. Broadband Electromagnetic Radiation Modulated by Dual Memristors, IEEE Antennas and Wireless Propagation Letters, (09 2011): 623. doi: 10.1109/LAWP.2011.2160038

TOTAL: 2

Number of Papers published in peer-reviewed journals:

(b) Papers published in non-peer-reviewed journals (N/A for none)

<u>Received</u>	<u>Paper</u>
-----------------	--------------

TOTAL:

Number of Papers published in non peer-reviewed journals:

(c) Presentations

Number of Presentations: 0.00

Non Peer-Reviewed Conference Proceeding publications (other than abstracts):

<u>Received</u>	<u>Paper</u>
-----------------	--------------

TOTAL:

Number of Non Peer-Reviewed Conference Proceeding publications (other than abstracts):

Peer-Reviewed Conference Proceeding publications (other than abstracts):

Received	Paper
2012/04/24 0` 3	L. Wang, Q. H. Liu. A Multi-Band Integrated Antenna Subsystem for Smartbook and Smartpad Applications, URSI Meeting, Toronto, Canada, July 2010.. 2010/07/03 00:00:00, . : ,
2012/04/24 0` 4	Q. H. Liu, L. Wang. A Dual-Frequency Printed Electrically Small Antenna Unit, URSI Meeting, Toronto, Canada, July 2010. 2010/07/03 00:00:00, . : ,
2012/04/24 0` 6	L. Wang, Q. H. Liu. Microstrip Patch Antenna Miniaturization Using the Impedance-Matched Magneto-Dielectric Substrate, URSI Meeting, Spokane, WA, July 2011.. 2011/07/03 00:00:00, . : ,
2012/04/24 0` 7	Lin Wang, Qing Huo Liu. Nonlinear Memristors Loaded Circular Loop Antenna, URSI Meeting, Spokane, WA, July 2011. 2011/07/03 00:00:00, . : ,
2012/04/24 0` 5	Y.-J. Ren, L. Wang, C.-H. Ahn, Q. H. Liu, K. Chang. Design of X-Band Wideband Linear Antenna Array with Reduced Number of Antenna Elements, URSI Meeting, Toronto, Canada, July 2010. 2010/07/03 00:00:00, . : ,

TOTAL: 5

Number of Peer-Reviewed Conference Proceeding publications (other than abstracts):

(d) Manuscripts

Received	Paper
TOTAL:	
Number of Manuscripts:	

Books

Received	Paper
TOTAL:	

Patents Submitted

Patents Awarded

Awards

Graduate Students

<u>NAME</u>	<u>PERCENT SUPPORTED</u>	Discipline
Lin Wang	0.80	
FTE Equivalent:	0.80	
Total Number:	1	

Names of Post Doctorates

<u>NAME</u>	<u>PERCENT SUPPORTED</u>
FTE Equivalent:	
Total Number:	

Names of Faculty Supported

<u>NAME</u>	<u>PERCENT SUPPORTED</u>	National Academy Member
William P. Joines	0.05	No
FTE Equivalent:	0.05	
Total Number:	1	

Names of Under Graduate students supported

<u>NAME</u>	<u>PERCENT SUPPORTED</u>
FTE Equivalent:	
Total Number:	

Student Metrics

This section only applies to graduating undergraduates supported by this agreement in this reporting period

- The number of undergraduates funded by this agreement who graduated during this period: 0.00
- The number of undergraduates funded by this agreement who graduated during this period with a degree in science, mathematics, engineering, or technology fields:..... 0.00
- The number of undergraduates funded by your agreement who graduated during this period and will continue to pursue a graduate or Ph.D. degree in science, mathematics, engineering, or technology fields:..... 0.00
- Number of graduating undergraduates who achieved a 3.5 GPA to 4.0 (4.0 max scale):..... 0.00
- Number of graduating undergraduates funded by a DoD funded Center of Excellence grant for Education, Research and Engineering:..... 0.00
- The number of undergraduates funded by your agreement who graduated during this period and intend to work for the Department of Defense 0.00
- The number of undergraduates funded by your agreement who graduated during this period and will receive scholarships or fellowships for further studies in science, mathematics, engineering or technology fields: 0.00

Names of Personnel receiving masters degrees

<u>NAME</u>
Total Number:

Names of personnel receiving PHDs

<u>NAME</u>
Total Number:

Names of other research staff

NAME

PERCENT_SUPPORTED

FTE Equivalent:

Total Number:

Sub Contractors (DD882)

1 a. Duke University, Office of Research Administration

1 b. 2200 West Main Street, Suite 820

Durham

NC

27705

Sub Contractor Numbers (c):

Patent Clause Number (d-1): 52.227-11

Patent Date (d-2): 12/1/2007 12:00:00AM

Work Description (e): Develop a multiscale software toll for field/circuitsimulation of communication devices

Sub Contract Award Date (f-1): 9/16/2009 12:00:00AM

Sub Contract Est Completion Date(f-2): 9/16/2010 12:00:00AM

Inventions (DD882)

Scientific Progress

Technology Transfer

Final Report for Contract W911NF-09-C-0159

A Multiscale Software Tool for Field/Circuit Co-Simulation

Wave Computation Technologies, Inc.

Dec. 15, 2011

Table of Contents

1. INTRODUCTION	5
1.1. Identification and Significance of the Problem.....	5
1.2. Available Field/Circuit Solvers in Research Community.....	6
1.3. Current Techniques to Address the Field Problem	7
1.4. The Proposed Multiscale Time-Domain Solver for Field/Circuit Simulation.....	8
2. SIMULATION METHODS	9
2.1. SETD and FETD Methods	9
2.1.1. SETD Method.....	9
2.1.2. FETD Method.....	10
2.1.3. Numerical Examples.....	11
2.2. Multi-Domain ECT Engine.....	13
2.2.1. Multi-Domain Methodology	13
2.2.2. Numerical Example	14
2.3. Multi-Circuit Simulation	16
2.3.1. Scheme to Support Multiple Circuits	16
2.3.2. Numerical Example	16
2.4. Hybrid SETD/FETD Method	18
2.4.1. Formulations	18
2.4.2. Numerical Example	20
2.5. Field-Circuit Applications.....	21
2.5.1. Single Stage Amplifier.....	21
2.5.2. Multiple Stage Amplifier	24
2.6. Hybrid SETD/FETD/ECT Method	26
2.6.1. Motivation to integrate the ECT method into the hybrid method	26

2.6.2.	Hybridization of SETD and ECT Methods.....	26
3.	Parallel Computation by Multiple Threads.....	29
3.1.	<i>Introduction of Parallelization</i>	<i>29</i>
3.2.	<i>Multidomain Parallelization</i>	<i>31</i>
3.3.	<i>Multidomain Balance</i>	<i>32</i>
3.4.	<i>Performance Speedup.....</i>	<i>34</i>
3.5.	<i>Numerical Results</i>	<i>36</i>
4.	PARALLEL COMPUTATION by GPU	39
4.1.	<i>Platforms</i>	<i>39</i>
4.2.	<i>GPU acceleration method on CUDA Engine</i>	<i>39</i>
4.3.	<i>GPU Acceleration Examples</i>	<i>41</i>
4.4.	<i>Implementation of PML subdomain</i>	<i>42</i>
4.5.	<i>Examples of PML subdomain</i>	<i>43</i>
5.	COMPREHENSIVE TESTINGS.....	46
5.1.	<i>Plane Wave Incident on a Large Domain.....</i>	<i>46</i>
5.2.	<i>Scattering of a Tilted Thin PEC Plate to an Electric Dipole Wave.....</i>	<i>47</i>
5.3.	<i>A Patch Antenna in a Reverberation Chamber</i>	<i>49</i>
5.4.	<i>A Tilted Parallel Wire Transmission Line Operated by Lumped Ports</i>	<i>50</i>
5.5.	<i>Wave propagation in a Room.....</i>	<i>52</i>
5.6.	<i>A Communication System</i>	<i>53</i>
5.7.	<i>A Patch Antenna Modulated by Dual Memristors</i>	<i>55</i>
5.8.	<i>Antenna Array.....</i>	<i>56</i>
5.9.	<i>Dual-Band Printed Electrically Small Antenna</i>	<i>58</i>
5.10.	<i>Simple Multiple-Channel Communication</i>	<i>60</i>
5.11.	<i>Complicated Multiple-Channel Communication</i>	<i>61</i>

6. CONCLUSION.....	64
REFERENCE	65

1. INTRODUCTION

The increasing levels of integration and miniaturization in military communications devices require the co-design of antennas and other electromagnetic elements with the baseband and drive circuitry. Field/circuit simulation is an important design prototyping step in research and development of such military communications devices. Time-domain techniques have significant advantages over the frequency-domain techniques for modeling nonlinear and time-varying components. However, no existing commercial EM simulation software can handle such complexity of co-simulation of complicated nonlinear circuitry in the field solver. This research will produce the first commercial software which can combine complex electromagnetic structures with nonlinear and dynamic circuitry in a multiscale manner by combining a circuit solver with a hybrid EM solver suitable for all scales (fine, intermediate, and coarse scales). This multiscale solver combines three efficient electromagnetic field algorithms, **(a)** the spectral element time-domain (SETD) method for coarse scale, **(b)** the enlarged cell technique (ECT) for the boundary conformal finite-difference time-domain method [i.e., the FDTD method improved to the second order in the presence of curved conductors] for intermediate scale, and **(c)** the finite-element time-domain (FETD) method for fine scale; the field solver is coupled with **(d)** a nonlinear circuit solver based on SPICE. The multiscale field solver is highly efficient for any mixed-scale problems.

1.1. Identification and Significance of the Problem

The co-design of antennas (and/or other electromagnetic elements) with the baseband and drive circuitry becomes increasingly important in today's military communications devices. A highly accurate and efficient combined field/circuit solver is essential for the successful design prototyping of these complex devices. Electromagnetic field/circuit solver codes have been used in the microwave research community, but none of the commercial software tools (such as HFSS of Ansoft or Microwave Studio of CST) can solve the combined field problem with nonlinear and dynamically changing circuit components. Therefore, the first problem is the development of the first commercial field/circuit solver prototype and its feasibility in the simulation of realistic devices. This is important because existing research codes in this area lack the user-friendliness and efficiency for fast prototyping.

The second problem is the low accuracy and efficiency in the FDTD method used in conventional field/circuit solvers in research community. As is now well known (also pointed out in [1] with a recent FDTD/circuit solver), the FDTD method suffers from the so-called staircasing errors because a curved surface is approximated by a staircased surface. Such staircasing errors make the computed electromagnetic fields near the curved surface zero-order accurate (i.e., the

accuracy does not improve as one refines the mesh), and globally at best first-order accurate because of super-convergence [2,3]. Consequently, if the sampling density (i.e., the number of points per wavelength, or PPWs) is doubled, the global numerical error decreases only by half. This is in stark contrast with the performance of the FDTD method in a homogeneous medium whose outer boundary aligns with the mesh – in that case the convergence is second order, i.e., if the sampling density is doubled, the global numerical error decreases by a factor of four. We will use our enlarged cell technique (ECT) to address this problem.

The third problem is the low efficiency in the conventional field solvers (and thus field/circuit solvers) for multiscale problems simultaneously with fine, intermediate, and coarse scales compared with the wavelength. The conventional FDTD and FETD (finite-element time-domain) methods are only feasible for small and intermediate scale problems because of their lower-order convergence. The high-order and spectral methods developed by this team are much more efficient for coarse-scale problems where the feature size of device structure is larger than a wavelength. In this project, we will combine three methods, i.e., the FETD method for the fine scale (where the feature size is smaller than 0.01 wavelengths), the ECT for the intermediate scale (where the feature size is between 0.01-2 wavelengths), and the SETD (spectral element time-domain) method for the coarse scale (where the feature size is larger than 2 wavelengths). This combined field solver is ideal for a multiscale problem where all three scales coexist; the discontinuous Galerkin method (DGM) will be used to combine these three methods in the field/circuit solver. Such a multiscale field/circuit solver will be especially advantageous for phased arrays with fine circuitry details.

1.2. Available Field/Circuit Solvers in Research Community

Currently available time-domain field/circuit solvers use three different methods for the field simulation: (a) the FDTD method, (b) the FETD method, and (c) the time-domain integral equation (TDIE) method. Sui et al. [4] introduce the FDTD and lumped circuits in 2D. The 3-D FDTD and circuit simulation is developed by Piket-May et al. [5]. Thomas et al. [6] propose to use SPICE with the FDTD method for field/circuit simulation. The time-consuming SPICE approach is avoided in the FDTD/circuit simulation through nonlinear solver based on the Newton-Raphson algorithm in [7-9]. The FETD method has been proposed in [10-12], and more recently the TDIE method has been developed in [13, 14]. The SPICE models can be found in [15, 16] with the Modified Nodal Analysis (MNA) Circuit Equations.

The major limitation of the FDTD/circuit solver is its low accuracy due to staircasing errors (see more discussions below). The FETD method is more accurate than FDTD method for curved and complex structures, but it is challenging for large-scale problems because a large mass matrix has to be inverted. The TDIE method still lags far behind in terms of its computation efficiency and thus significant more research has to be done before it becomes practical.

1.3. Current Techniques to Address the Field Problem

In the computational electromagnetics (CEM) community, recently at least three classes of techniques have been developed to address the large staircasing errors in the FDTD method: (a) the body fitted coordinates [18], (b) fractional cell, mixed boundary elements, or embedded boundaries [2,3,17,19,20], and (c) fully unstructured mesh techniques [21-28]. The first two methods [(a) and (b)] can achieve second-order accuracy, while the third technique [(c)] can potentially achieve spectral accuracy (i.e., the error decreases exponentially with the sampling density). In comparison, techniques in (b) are easier to implement than techniques in (a), and apply to more complicated structures. Our numerical results confirmed that the ECT improves the FDTD method to second-order accuracy. Furthermore, at the same 5% accuracy requirement, the ECT requires only 8 PPWs, while the FDTD method requires 80 PPWs (10 times denser sampling); thus, the ECT is approximately 1000 times more efficient than FDTD for such a problem in 3D.

The techniques in class (c) above include the discontinuous Galerkin method and multidomain pseudospectral time-domain (PSTD) method. The main advantage of these techniques is their spectral accuracy (thus very low sampling density) for electrically large domains (i.e., domains with structures large compared to the wavelength). We have developed both DGM [30] and PSTD methods [23-28] and showed that these methods require only about 3-4 points per wavelength. On the other hand, they are not suitable for electrically fine regions where the geometrical features are much smaller than wavelength ($< \frac{1}{4}$ wavelength), because at this sub-wavelength regime lower-order methods (such as the FDTD or its improved versions) are already accurate enough and less expensive because the methods in (c) have some overhead associated with the interface treatment.

Recently, we have developed the spectral-element time-domain (SETD) method [31] by using the Gauss-Lobatto-Legendre (GLL) polynomials as the basis functions and GLL points as the quadrature integration points. This yields a block-diagonal mass matrix, which is much more efficient than that in the finite element time-domain method where the mass matrix is not block-diagonal. Compared to the PSTD method or spectral DGM, this SETD method does not have the overhead associated with the interface treatment for each element. To treat problems with different scales, we have also incorporated the discontinuous Galerkin method to the SETD method to allow multidomain treatment (see [32]). Therefore, the SETD method can be viewed as an improved method compared to the multidomain PSTD method.

In summary, these more advanced methods proposed to overcome the limitations of the conventional FDTD method have problem dependent advantages and disadvantages.

1.4. The Proposed Multiscale Time-Domain Solver for Field/Circuit Simulation

In view of the advantages and disadvantages of the above new techniques, we proposed to develop a hybrid method that combines (a) the SETD method (Lee and Liu [31,32]) with (b) the second-order accurate enlarged cell technique ([17,29]), and (c) the FETD method for very fine details. Specifically, the SETD method will be used in electrically large regions so that the sampling density there can be greatly reduced, while the ECT method will be used in regions that have sub-wavelength fine geometrical features. The FETD method is for even finer structures where the explicit time integration in ECT is not efficient. The interface between different regions will be treated by the discontinuous Galerkin method where the flux is correctly updated to ensure stability.

For any given field/circuit problem, one can divide the problem geometry into two classes, (a) one with sub-wavelength fine structures where the ECT (boundary-conformal FDTD) method will be utilized, and (b) one without sub-wavelength structures where the SETD method will be used to allow coarse sampling. The interface conditions will be treated by correctly accounting for electromagnetic fluxes with the discontinuous Galerkin approach (Riemann solver).

2. SIMULATION METHODS

In this section, we will give all simulation methods for the multiscale problems. We will first present the formulation of the SETD and FETD. Next, Multi-Domain ECT and Multi-Circuit will be presented. And then the hybridization of SETD, FETD, and ECT will be followed.

2.1. SETD and FETD Methods

In this section, we will give a brief introduction to the multiscale hybrid method combining the SETD and FETD methods. The governing equations are Maxwell's equations, as shown in Eq. (2.1) and (2.2), where the electric field \mathbf{E} and magnetic field \mathbf{H} are normalized by $\tilde{\mathbf{E}} = \mathbf{E}/\sqrt{\mu_0}$ and $\tilde{\mathbf{H}} = \mathbf{H}/\sqrt{\epsilon_0}$.

$$\epsilon_r \frac{\partial \tilde{\mathbf{E}}}{\partial t} = c_0 \nabla \times \tilde{\mathbf{H}} - \frac{\sigma}{\epsilon_0} \tilde{\mathbf{E}} - \frac{\mathbf{J}_s}{\epsilon_0 \sqrt{\mu_0}} \quad (2.1)$$

$$\mu_r \frac{\partial \tilde{\mathbf{H}}}{\partial t} = -c_0 \nabla \times \tilde{\mathbf{E}} \quad (2.2)$$

2.1.1. SETD Method

The spectral element time-domain (SETD) method is an efficient and accurate high-order method allowing coarse sampling for electrically-large structures. In this method, Maxwell's equations are discretized as

$$\begin{aligned} \epsilon_r \frac{d}{dt} \int_{\Omega} \tilde{\mathbf{E}} \cdot \Phi_i \, d\Omega &= c_0 \int_{\Omega} \tilde{\mathbf{H}} \cdot (\nabla \times \Phi_i) \, d\Omega \\ &\quad - \frac{\sigma}{\epsilon_0} \int_{\Omega} \tilde{\mathbf{E}} \cdot \Phi_i \, d\Omega - \frac{1}{\epsilon_0 \sqrt{\mu_0}} \int_{\Omega} \mathbf{J}_s \cdot \Phi_i \, d\Omega \\ &\quad + c_0 \int_{\partial\Omega} (\hat{n} \times \tilde{\mathbf{H}}) \cdot \Phi_i \, ds \end{aligned} \quad (2.3)$$

$$\begin{aligned} \mu_r \frac{d}{dt} \int_{\Omega} \tilde{\mathbf{H}} \cdot \boldsymbol{\Psi}_i d\Omega &= -c_0 \int_{\Omega} \tilde{\mathbf{E}} \cdot (\nabla \times \boldsymbol{\Psi}_i) d\Omega \\ &\quad - c_0 \int_{\partial\Omega} (\hat{n} \times \tilde{\mathbf{E}}) \cdot \boldsymbol{\Psi}_i ds \end{aligned} \quad (2.4)$$

where $\boldsymbol{\Phi}_i$ and $\boldsymbol{\Psi}_i$ are basis functions based on the Gauss–Lobatto–Legendre polynomials for $\tilde{\mathbf{E}}$ and $\tilde{\mathbf{H}}$, respectively.

To model an arbitrary hexahedron element, a reference element of cube is usually introduced. The mapping between the hexahedron and the reference cube is as following

$$\begin{aligned} \boldsymbol{\Phi} &= \mathbf{J}^{-1} \hat{\boldsymbol{\Phi}} \\ \nabla \times \boldsymbol{\Phi} &= \frac{1}{|\mathbf{J}|} \mathbf{J}^T \hat{\nabla} \times \hat{\boldsymbol{\Phi}} \end{aligned} \quad (2.5)$$

where $\boldsymbol{\Phi}$ and $\hat{\boldsymbol{\Phi}}$ represent the basis functions in the hexahedron element and in the reference element, respectively. And

$$\hat{\boldsymbol{\Phi}}_{mnp}^{a_i} = \hat{\boldsymbol{\Psi}}_{mnp}^{a_i} = \hat{a}_i \phi_m^{(N)}(\xi) \phi_n^{(N)}(\eta) \phi_p^{(N)}(\zeta) \quad (2.6)$$

and \mathbf{J} is the Jacobian matrix defined as

$$\mathbf{J} = \begin{bmatrix} \frac{\partial x}{\partial \xi} & \frac{\partial y}{\partial \xi} & \frac{\partial z}{\partial \xi} \\ \frac{\partial x}{\partial \eta} & \frac{\partial y}{\partial \eta} & \frac{\partial z}{\partial \eta} \\ \frac{\partial x}{\partial \zeta} & \frac{\partial y}{\partial \zeta} & \frac{\partial z}{\partial \zeta} \end{bmatrix} \quad (2.7)$$

2.1.2. FETD Method

The finite element time-domain (FETD) method is an efficient method for complex electrically fine structures. Its discretization of Maxwell's equation is similar to the SETD method. For example, the equation to update $\tilde{\mathbf{E}}$ is shown in Eq. (2.8).

$$\begin{aligned} \epsilon_r \frac{d}{dt} \int_{\Omega} \tilde{\mathbf{E}} \cdot \mathbf{N}_i^e d\Omega &= -\frac{\sigma}{\epsilon_0} \int_{\Omega} \tilde{\mathbf{E}} \cdot \mathbf{N}_i d\Omega - \frac{1}{\epsilon_0 \sqrt{\mu_0}} \int_{\Omega} \mathbf{J}_s \cdot \mathbf{N}_i d\Omega \\ &\quad + c_0 \int_{\Omega} \tilde{\mathbf{H}} \cdot (\nabla \times \mathbf{N}_i^e) d\Omega \\ &\quad + c_0 \int_{\partial\Omega} (\hat{n} \times \tilde{\mathbf{H}}) \cdot \mathbf{N}_i^e ds \end{aligned} \quad (2.8)$$

The differences between the FETD and SETD methods come from the basis and test functions and the element shape, where tetrahedron may also be considered. In the FETD method, mixed-order basis functions are considered, such as \mathbf{N}_i^e and \mathbf{N}_i^h for $\tilde{\mathbf{E}}$ and $\tilde{\mathbf{H}}$, respectively. For example, the vector basis functions for hexahedron element in FETD are defined as

$$\hat{\mathbf{N}}^e = \begin{Bmatrix} \phi_m^{(0)}(\xi) \phi_n^{(1)}(\eta) \phi_p^{(1)}(\zeta) \hat{\xi} \\ \phi_m^{(1)}(\eta) \phi_n^{(0)}(\eta) \phi_p^{(1)}(\zeta) \hat{\eta} \\ \phi_m^{(1)}(\zeta) \phi_n^{(1)}(\eta) \phi_p^{(0)}(\zeta) \hat{\zeta} \end{Bmatrix} \quad (2.9)$$

$$\hat{\mathbf{N}}^h = \begin{Bmatrix} \phi_m^{(1)}(\xi) \phi_n^{(2)}(\eta) \phi_p^{(2)}(\zeta) \hat{\xi} \\ \phi_m^{(2)}(\eta) \phi_n^{(1)}(\eta) \phi_p^{(2)}(\zeta) \hat{\eta} \\ \phi_m^{(2)}(\zeta) \phi_n^{(2)}(\eta) \phi_p^{(1)}(\zeta) \hat{\zeta} \end{Bmatrix} \quad (2.10)$$

The discontinuous Galerkin (DG) method is employed to hybridize two different methods across an interface. Several kinds of DG operators can be used for the boundary integral items over interfaces between different sub-domains. Each DG operator has its own advantages and disadvantages. Here, we demonstrate how to communicate the two FETD and SETD domain by the center flux in a DG method, the two boundary integral items on an interface will be determined by the average of field values of two sub-domains adjacent to the interfaces, i.e.

$$\int_S \mathbf{N}_e^{(i)} \cdot \hat{\mathbf{n}}^{(i)} \times \mathbf{H} dS = \frac{1}{2} \int_S \mathbf{N}_e^{(i)} \cdot \hat{\mathbf{n}}^{(i)} \times \mathbf{H}^{(i)} dS + \frac{1}{2} \int_S \mathbf{N}_e^{(i)} \cdot \hat{\mathbf{n}}^{(i)} \times \mathbf{H}^+ dS \quad (2.11)$$

$$\int_S \mathbf{N}_h^{(i)} \cdot \hat{\mathbf{n}}^{(i)} \times \mathbf{E} dS = \frac{1}{2} \int_S \mathbf{N}_h^{(i)} \cdot \hat{\mathbf{n}}^{(i)} \times \mathbf{E}^{(i)} dS + \frac{1}{2} \int_S \mathbf{N}_h^{(i)} \cdot \hat{\mathbf{n}}^{(i)} \times \mathbf{E}^+ dS \quad (2.12)$$

where $\mathbf{E}^{(i)}$ and $\mathbf{H}^{(i)}$ fields are from the local sub-domain, viz. the i th sub-domain, and \mathbf{E}^+ and \mathbf{H}^+ are from neighbor sub-domains.

2.1.3. Numerical Examples

The first example is a simple metallic cavity case. It is used to verify our FETD code. A TE101 mode is excited and the Ez fields are recorded at an observation point. The results are compared with FDTD results, as shown in Fig. 2.1.

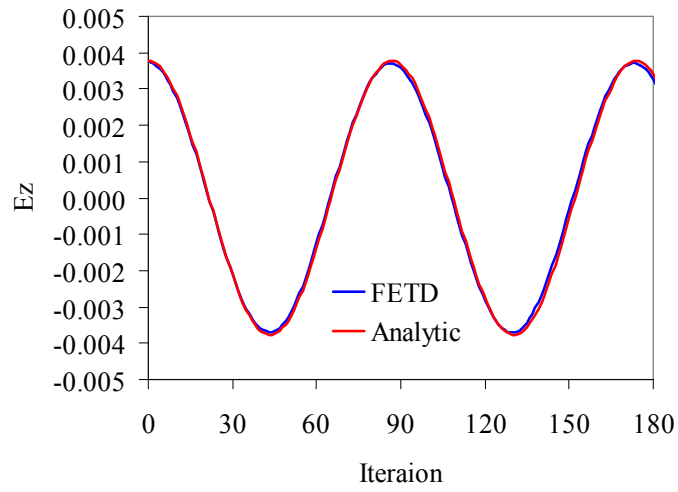


Fig. 2.1: A metallic cavity excited by TE101 mode.

The second example involves a dielectric, which is impinged by a plane wave. The geometry is shown in Fig. 2.2 Left. And the SETD results are shown in Fig. 2.2 Right. The comparison with the ECT results is used to verify our SETD code.

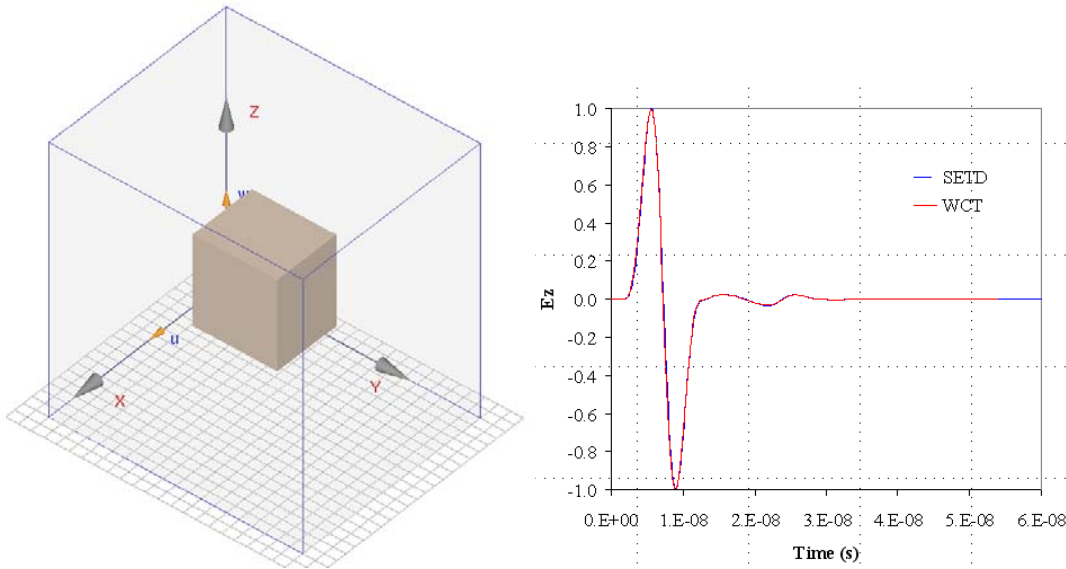


Fig. 2.2: Left: a dielectric is impinged by a plane wave. Right: E_z fields recorded at an observation point.

2.2. Multi-Domain ECT Engine

The ECT (Enlarged Cell Technique) engine is used for the field simulation in our software. It is an improved conformal FDTD simulation solver without the need to reduce the time step for irregular cells. As is well known, the FDTD solver can be easily modified for parallel computation by dividing its total computational domain into a number of sub-domains. And so is the ECT engine.

2.2.1. Multi-Domain Methodology

Here we briefly discuss about our methodology to divide the computational domain and to communicate among adjacent sub-domains. Several issues have to be considered: domain partition, domain communication and element locating. For the domain partition, we choose a simple but practical and robust strategy. For our multi-domain computation, the total computational domain is divided into a number of sub-domain segments in each of the three Cartesian directions in a structured manner with $N_x \times N_y \times N_z$ sub-domains. For example, the total domain is divided into $3 \times 4 \times 5$ sub-domains, with 3 domain segments in the x direction, 4 in the y direction, and 5 in the z direction. All sub-domains are aligned to their adjacent domains horizontally or vertically. Such a structured layout of sub-domains in the regular partition makes the bookkeeping of sub-domains very simple and efficient, because an efficient data structure of 3-D array can be used to record all the sub-domains. For example, the array element (2, 3, 4) can be used to denote the sub-domain which is at the 2nd place in the x direction, 3rd place in the y direction and 4th place in the z direction. In addition, each sub-domain has its own memory allocation of its field components and supporting data for an efficient use of memory and a good performance of computational time.

For the sub-domain communication, we have to consider a specialty of the staggered grid used in the ECT engine, where E field components and H field components are displaced by half a cell, as shown in Fig. 2.3.

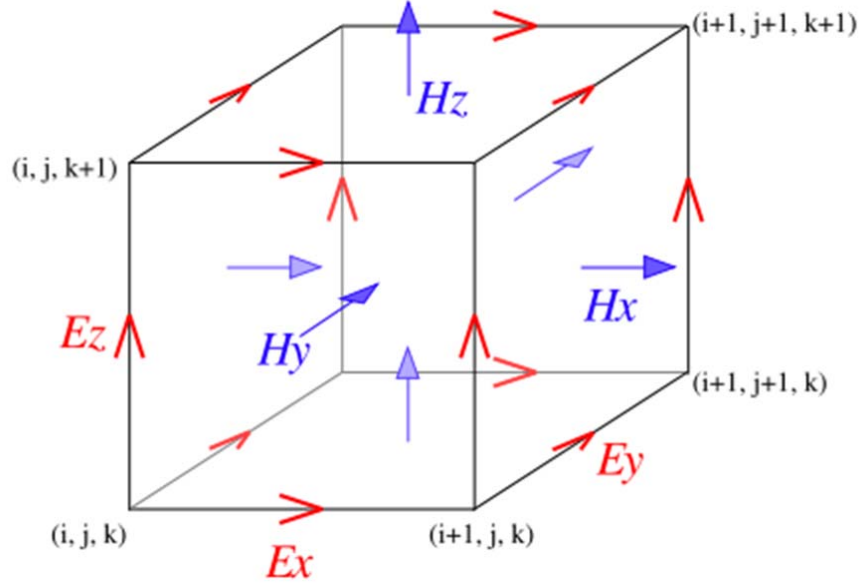


Fig. 2.3: A cell in the staggered grid is illustrated, where E field components and H field components are displaced by half a cell.

A symmetric scheme is constructed for the sub-domain communication. We assume the left walls are E walls, and right walls are H walls. In other words, on the left surface of the sub-domain, the E tangential components are located, while on the right surface of the sub-domain, the H tangential components are located, as shown in Fig. 2.3. And the tangential fields on the boundary walls will be obtained by transferring from its adjacent sub-domains. An elemental loop of the time stepping including the adjacent sub-domain communication is as follows:

- (1) Update the E field in each sub-domain.
- (2) Transfer the E field from the left sub-domains to the right sub-domains.
- (3) Update the H field in each sub-domain.
- (4) Transfer the H field from the right sub-domains to the left sub-domains.

To locate an element, such as a source, an observer, and so on, we have to find first in which sub-domain it is and then find in which cell it is in that sub-domain.

2.2.2. Numerical Example

A patch antenna as shown in Fig. 2.4 is used here to verify our development of multi-domain ECT engine. It is fed by a transmission line of characteristic impedance of 50 ohm. The total domain is divided into 4 sub-domains along the y direction. The scattering parameter S11 is calculated. And its result is plotted in Fig. 2.5. To verify the result, a single domain simulation is

also performed. We can easily see that the two results agree very well. This confirms that the multidomain ECT method works well for antenna problems.

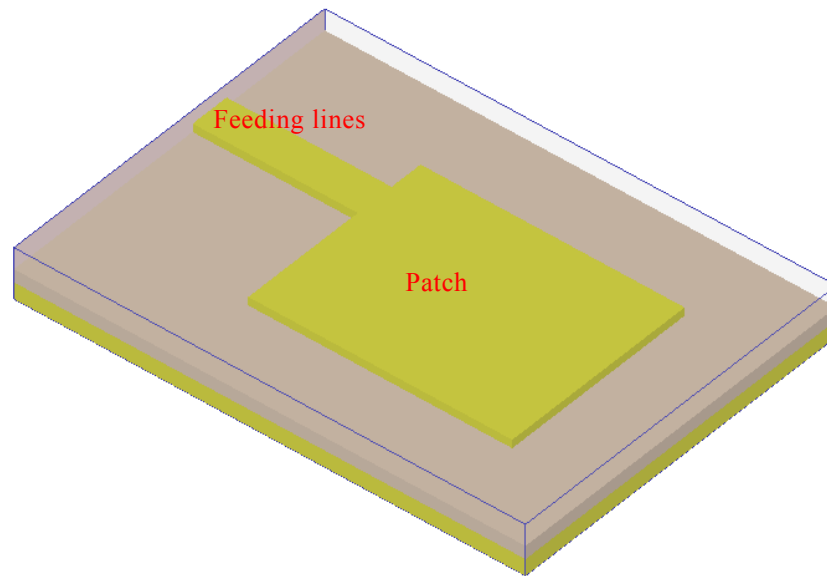


Fig. 2.4: A patch antenna is fed by a transmission line of 50 ohm.

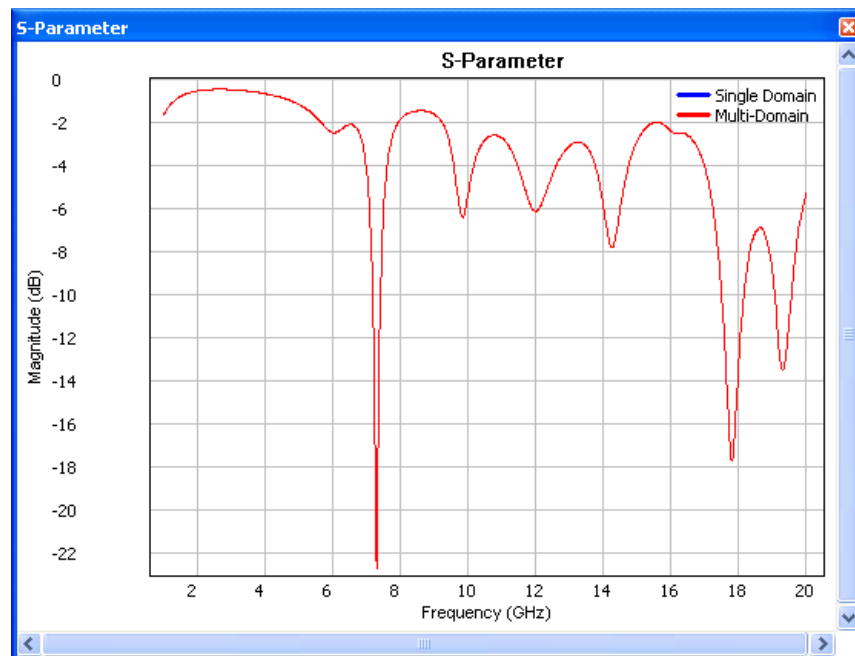


Fig. 2.5: Comparison of S11 parameter results for a multi-domain and a single domain simulation for the patch antenna. The two results completely overlap.

2.3. Multi-Circuit Simulation

To extend the application domain of our software in circuit/field co-simulation, we have added a new feature to support multiple circuits, especially multiple SPICE circuits.

2.3.1. Scheme to Support Multiple Circuits

First, we will introduce our scheme to support multiple circuits. Two circuit solvers are provided in our software for the field/circuit co-simulation: the internal circuit solver for some simple circuit elements and the SPICE circuit solver for arbitrarily complex circuits. For the internal circuit solver, there is no difficulty to support multiple circuits as long as two circuit elements are not defined at the same position. However, for the SPICE circuit solver, an extra work is required to support multiple circuits since the third-party SPICE library is employed in our package. Currently, a simple way is applied, which solve the multiple circuits sequentially at each time step of the ECT. The Norton equivalent circuit method is used to link the SPICE and ECT cell. At each time step, the updating scheme is shown as follows.

1. The current I_N for each circuit, as shown in Fig. 2.6, is computed at time step $n+1/2$ using the H field circulated around the cell containing the device port.
2. The SPICE circuit solver is used to model the circuits one by one with $I_N^{n+1/2}$ obtained in step 1 as an excitation. This step updates V_{dev}^n to V_{dev}^{n+1} , thereby E^{n+1} components at the device port is obtained.
3. Use the normal ECT scheme to update the E field elsewhere.
4. Use the normal ECT scheme to update the H field from $n+1/2$ time step to $n+3/2$ time step.

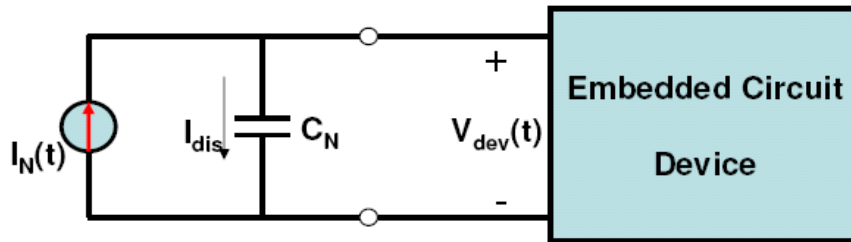


Fig. 2.6: The i -th circuit device embedded in a cell of the ECT grid and the Norton equivalent circuit looking into the ECT grid from this port.

2.3.2. Numerical Example

To verify the scheme of multi-circuit simulation a radio frequency signal amplifier, as show in Fig 2.7, is modeled by a SPICE circuit. The basic geometry is shown in Fig. 2.7, where a patch

antenna is used to receive electromagnetic signal. And the signal is transmitted by a coaxial cable. An amplification circuit is used to connect the inner and outer conductor of the coaxial cable to amplify the transmitted signal, as shown in Fig. 2.8.

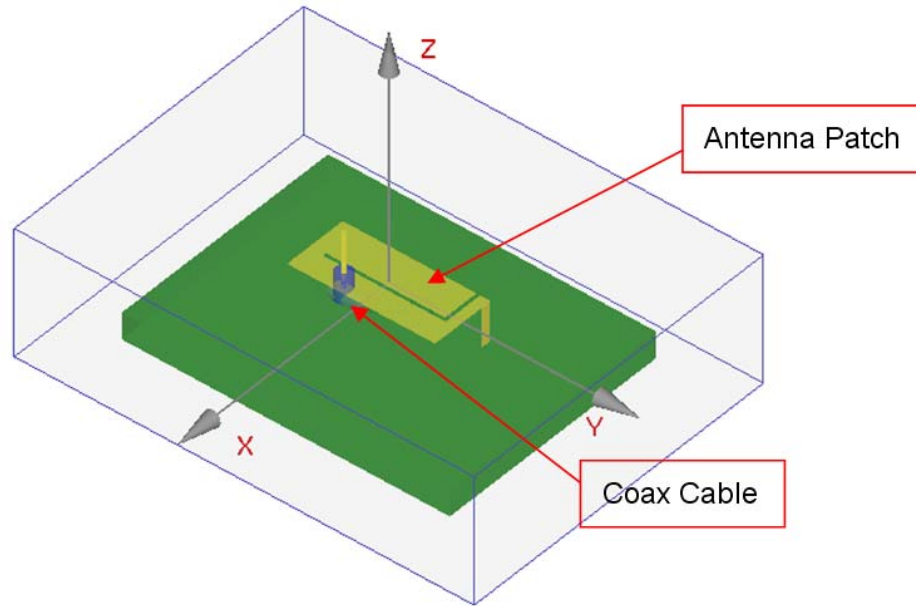


Fig. 2.7: The basic geometry of the radio frequency signal amplifier. It includes a patch antenna to receive an electromagnetic wave and a coaxial cable to transmit the received signals.

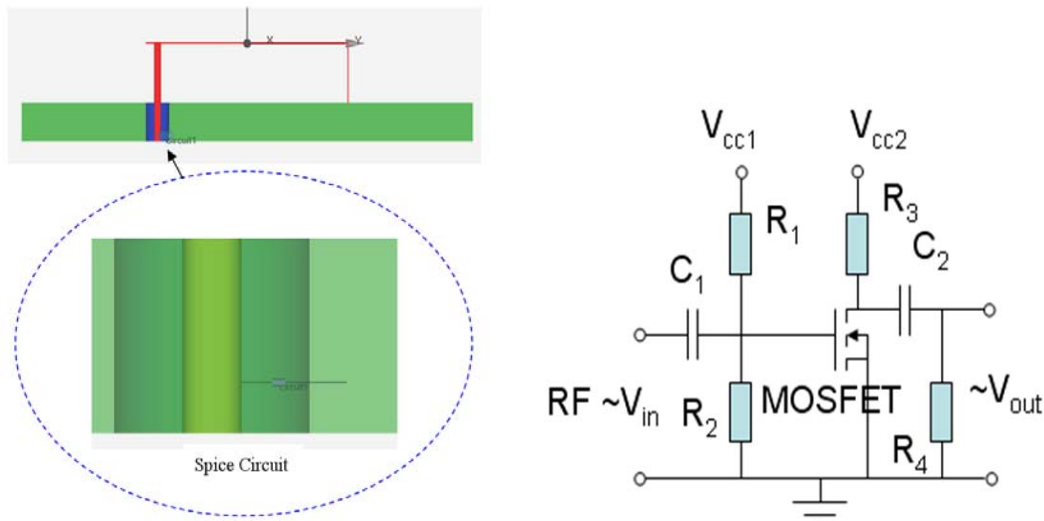


Fig. 2.8: Left: An amplification magnifier is built to connect the inner and outer conductor of the transmitted coaxial cable. Right: the amplification circuit with $v_{cc1} = v_{cc2} = 10 \text{ V}$. C_1 and C_2 are coupling capacitors with a same value of $1 \mu\text{F}$. R_1 and R_2 are DC bias resistors with a same value of $1 \text{ M}\Omega$. $R_3 = 35\text{k}\Omega$, $R_4 = 100\text{M}\Omega$. The MOSFET is N channel BSIM2.

A plane wave of frequency 2.4 GHz and amplitude 10 V/m is used to model the electromagnetic signal. The voltage received at the coax cable is recorded. Two results are compared with and without the using of the amplification circuit. We can clearly see from Fig. 2.9 that the effect of the amplification.

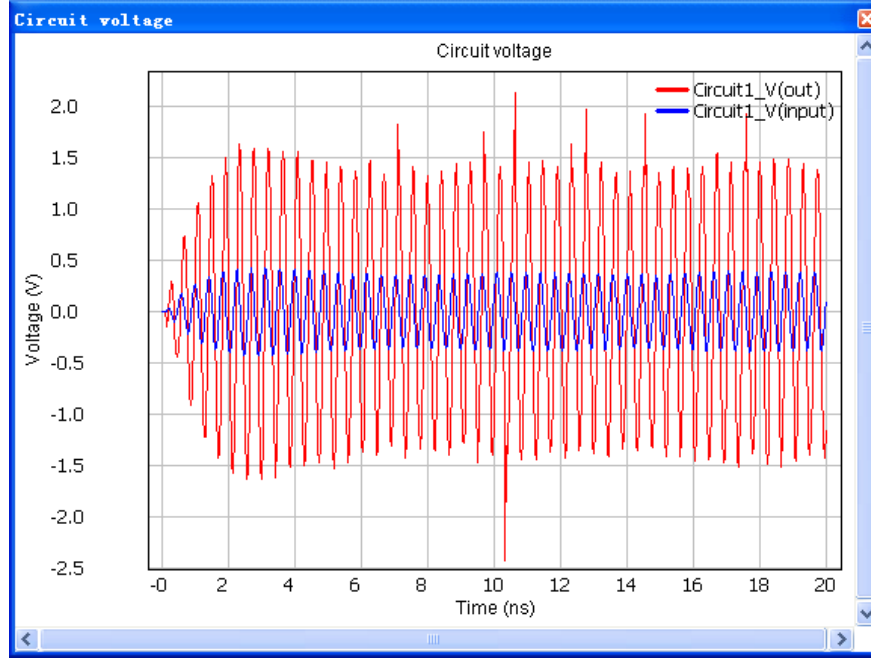


Fig. 2.9: Voltages received with and without the amplification circuit. The blue curve is the input signal to the amplification circuit, which is in fact the signal received without the use of the amplification circuit.

2.4. Hybrid SETD/FETD Method

2.4.1. Formulations

Field-circuit applications involve multiple scales and complex geometries. Usually the circuit regions have electrically small scales and complex geometries, while the field propagation regions have electrically large scales and simple geometries. A hybrid method, when set up appropriately, can significantly outperform any individual methodology for a complex multiscale problem. Considering the geometrical features of field-circuit applications, we developed a hybrid SETD/FETD method for their simulation. To apply this hybrid method, the computational domain is divided into a number of sub-domains according to their electrical scale properties. The SETD method is assigned to electrically large sub-domains to allow a very coarse sampling for efficiency; while the FETD method is assigned to electrically small sub-domains with fine and complex structures. Structured cuboid meshes are used in the SETD sub-domains; while unstructured tetrahedron meshes are used in the FETD sub-domains. The most important advantage of our

hybrid method is that the meshes in the different sub-domains can be generated independently. This alleviates the mesh generation difficulties with large multiscale problems in the finite element method (FEM).

The discontinuous Galerkin (DG) method is employed to coupling two different methods across an interface. It basically implements the surface integration in the weak forms of Maxwell's equations in the FEM context by using fields in both side of the interface. The weak forms of Maxwell's equations are shown in Eq. (2.13) and (2.14):

$$\begin{aligned} \epsilon_r \frac{d}{dt} \int_{\Omega} \tilde{\mathbf{E}} \cdot \Phi_i \, d\Omega &= c_0 \int_{\Omega} \tilde{\mathbf{H}} \cdot (\nabla \times \Phi_i) \, d\Omega \\ &\quad - \frac{\sigma}{\epsilon_0} \int_{\Omega} \tilde{\mathbf{E}} \cdot \Phi_i \, d\Omega - \frac{1}{\epsilon_0 \sqrt{\mu_0}} \int_{\Omega} \mathbf{J}_s \cdot \Phi_i \, d\Omega \\ &\quad + c_0 \int_{\partial\Omega} (\hat{n} \times \tilde{\mathbf{H}}) \cdot \Phi_i \, ds \end{aligned} \quad (2.13)$$

$$\begin{aligned} \mu_r \frac{d}{dt} \int_{\Omega} \tilde{\mathbf{H}} \cdot \Psi_i \, d\Omega &= -c_0 \int_{\Omega} \tilde{\mathbf{E}} \cdot (\nabla \times \Psi_i) \, d\Omega \\ &\quad - c_0 \int_{\partial\Omega} (\hat{n} \times \tilde{\mathbf{E}}) \cdot \Psi_i \, ds \end{aligned} \quad (2.14)$$

And Riemann solver Eq. (2.15) and (2.16) are used to couple the fields on both sides of the interface:

$$\begin{aligned} &(\hat{n} \times \mathbf{H})(Z^{(1)} + Z^{(2)}) \\ &= \hat{n} \times \left(Z^{(1)} \mathbf{H}^{(1)} + \hat{n} \times \mathbf{E}^{(1)} \eta_0 + Z^{(2)} \mathbf{H}^{(2)} - \hat{n} \times \mathbf{E}^{(2)} \eta_0 \right) \end{aligned} \quad (2.15)$$

$$\begin{aligned} &(\hat{n} \times \mathbf{E})(Y^{(1)} + Y^{(2)}) \\ &= \hat{n} \times \left(Y^{(1)} \mathbf{E}^{(1)} - \hat{n} \times \frac{\mathbf{H}^{(1)}}{\eta_0} + Y^{(2)} \mathbf{E}^{(2)} + \hat{n} \times \frac{\mathbf{H}^{(2)}}{\eta_0} \right) \end{aligned} \quad (2.16)$$

The surface integration between two different sub-domains requires an analysis of the element shape relationship when a non-conformal (non-matched) mesh exists at the interface. For example, on an interface of an SETD sub-domain and a FETD sub-domain, the relation of a rectangle element and a triangle element has to be considered. The triangle and rectangle elements have many geometric relations. We have successfully analyzed the elemental shape relations in all kinds of situations. Integration over the shared area of polygon is required in the hybrid SETD/FETD method. To integrate, we split the polygon into several triangles, because the Gaussian quadrature over a triangle is well known, and can be used to perform the numerical integration readily.

2.4.2. Numerical Example

The example is a plane wave incident on two distant scatterers. One is a PEC sphere located at the left-bottom-front corner, while the other is a PEC cylinder located at the right-top-back corner. The two scatterers are purposely placed far away to simulate a multi-scale situation. The sizes of the scatters are around half of a wavelength. The distance between them is about 3 wavelengths. FETD sub-domains are assigned around the small scatterers, as shown in Fig. 2.10, while the other space is divided into SETD sub-domains.

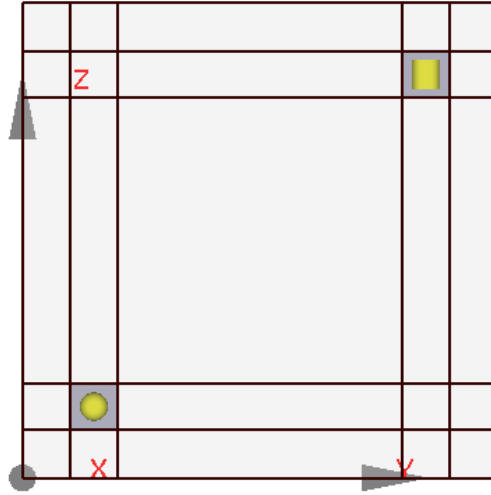


Fig. 2.10: The total computational domain is divided into 125 sub-domains with 5 partitions in each direction. Two FETD sub-domains are assigned around the two small scatterers, while the others are SETD sub-domains. PML is used to absorb outgoing waves at the computational edge.

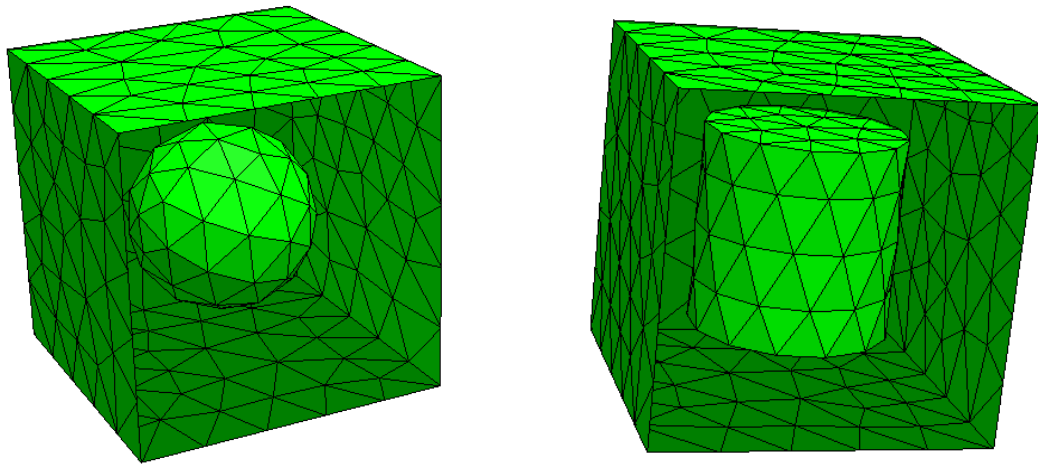


Fig. 2.11: The tetrahedron meshes of the two FETD sub-domains. The left is for the left-lower-front FETD sub-domain with a PEC sphere scatterer. The right is for the right-top-back FETD sub-domain with a PEC cylinder scatterer.

The tetrahedron meshes of the two FETD sub-domains are shown in Fig. 2.11. A plane wave propagating along the X direction is incident on the two scatterers. The electric field of the plane wave is polarized along the Z direction. Two observers are placed to record the Ez field component. The results are compared with the FDTD results. Again, excellent agreement is obtained as shown in Fig. 2.12.

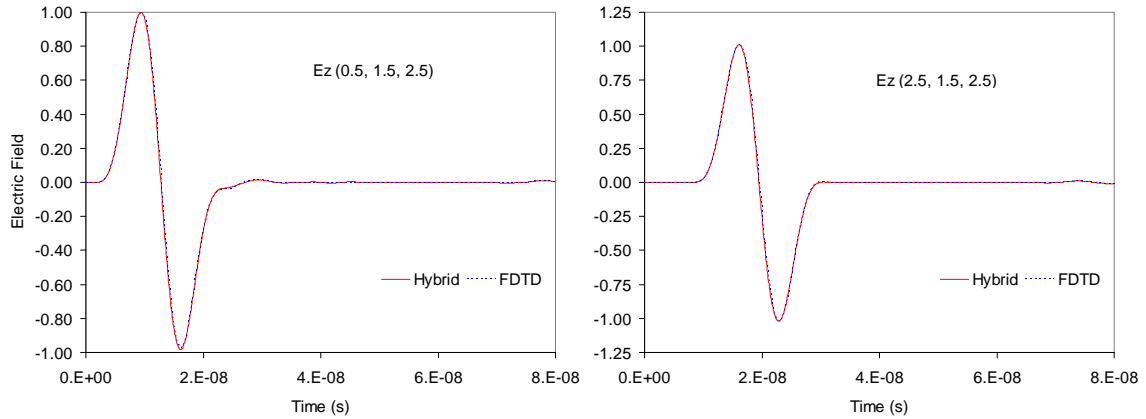


Fig. 2.12: The Ez field at the two observers located at (0.5, 1.5, 2.5) m and (2.5, 1.5, 2.5) m. Excellent agreement is obtained by comparing with the reference FDTD results.

2.5. Field-Circuit Applications

We have demonstrated some field-circuit applications with our software. The applications include: (1) single stage amplifier; (2) multiple (2 and 3) stage amplifiers. The first application is from the paper [33] so that we can compare our results with those reference results. Good agreement of our results to those in the reference paper is obtained. It shows that our software can successfully simulate such complex field-circuit applications.

2.5.1. Single Stage Amplifier

The first application is a single stage microwave FET amplifier. The simulation structure consists of a microwave FET and a microstrip line. Fig. 2.13 shows the configuration of the microwave FET amplifier in WCT modeling environment. The gray box is the FDTD simulation area. Details of geometry parameters of the active device are given in Fig. 2.14, where the amplifier is connected between points A and B.

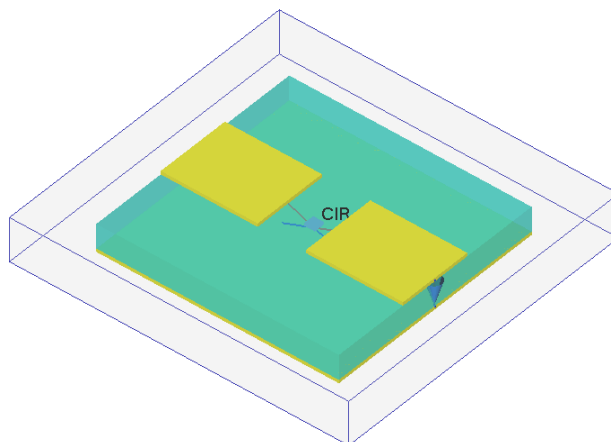


Fig. 2.13: The perspective view in Wavenology EM for a microwave amplifier connected to a microstrip line.

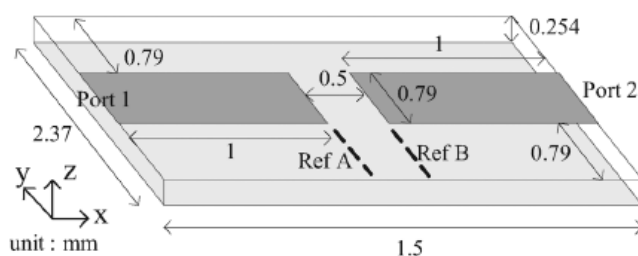


Fig. 2.14: Detail parameters of the microstrip and a linear microwave amplifier in Fig. 2.13.

The small signal equivalent circuit of the FET is given in Fig. 2.15.

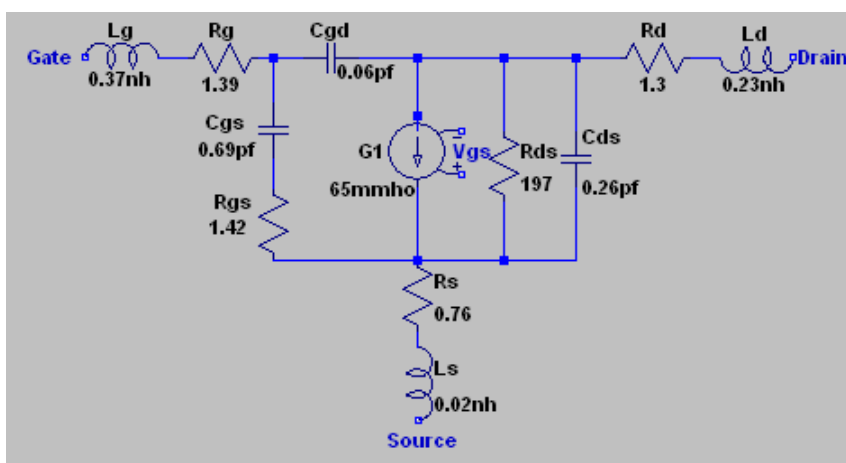


Fig. 2.15: The small signal equivalent circuit of a common-source microwave FET.

We use the cell size in the X and Y directions as $\Delta x = 0.1$ mm and $\Delta y = 0.079$ mm. In the Z direction, we have five computation cells for the dielectric substrate since Wavenology EM uses a nonuniform gridding scheme. The time step increment is 0.09 ps, which is smaller than the reference value of 0.16 ps in [33]. The dielectric constant of the substrate is 2.17. A BHW pulse time function is applied at Lumped Port 1 on the left end of the microstrip line. The observation port is Lumped Port 2 on the right end of the microstrip line.

The simulated S-parameters, S11 and S21, of the active microwave amplifier circuit are shown in Figs. 2.17 and 2.18, respectively, from 1 GHz to 15 GHz. The results from FDTD [33] and ADS Agilent's Advanced Design System (ADS) were provided for comparison. Good agreement is achieved between the method from FDTD [33] and Wavenology EM. The small difference from ADS is due to the lack of full wave analysis capability of ADS.

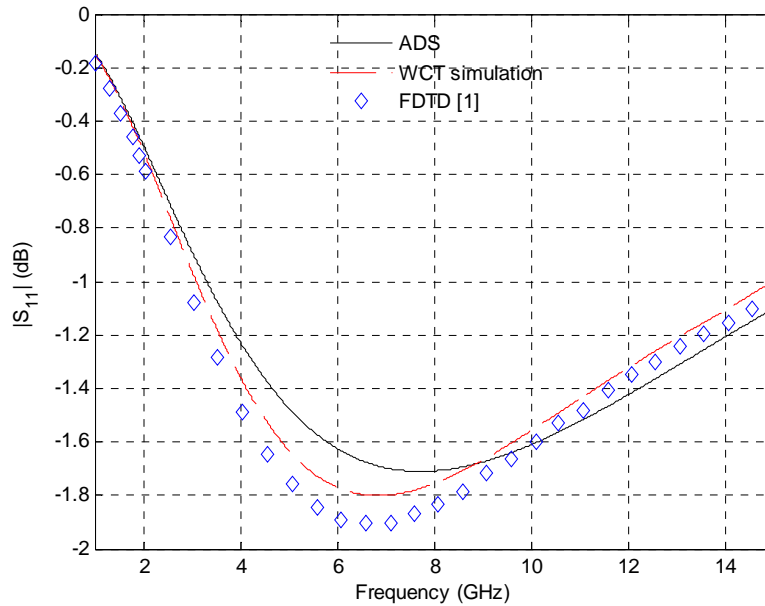


Fig. 2.17: Magnitude of the S11 of the amplifier circuit in Fig. 2.13 compared with the FDTD [1] and ADS results.

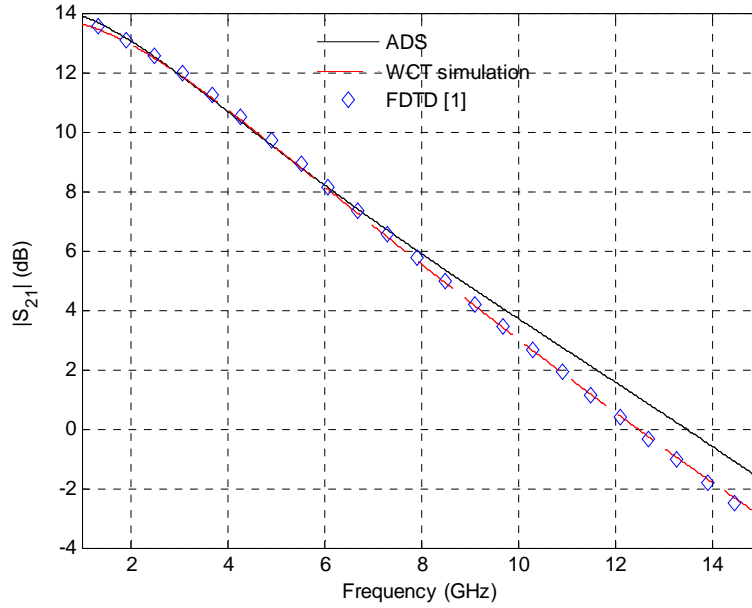


Fig. 2.18: Magnitude of the S21 of the amplifier circuit in Fig. 2.13 compared with the FDTD [33] and ADS.

2.5.2. Multiple Stage Amplifier

To demonstrate our software's capabilities in simulating complex multiple-stage amplifiers in particular, and multiple circuits in general, the two- and three-stage amplifier cases, as shown in Fig. 2.19 and 2.20, are considered.

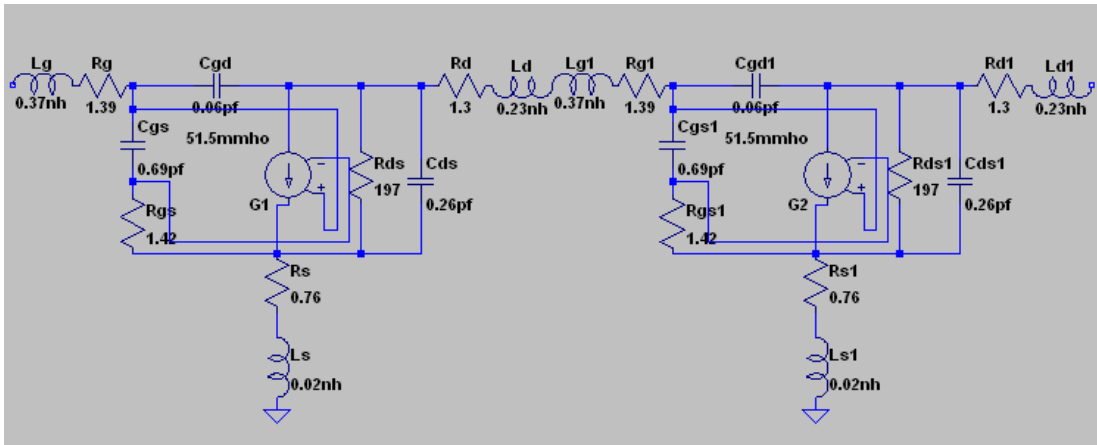


Fig. 2.19: The small signal equivalent circuit for a two-stage amplifier configuration.

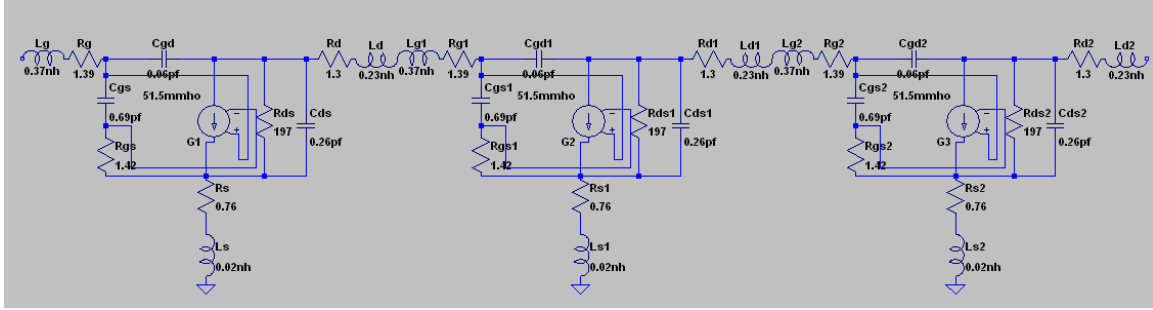


Fig. 2.20: The small signal equivalent circuit for a three-stage amplifier configuration.

Figs. 2.19 and 2.20 give the small-signal equivalent circuit models for the two- and three-stage amplifiers, which are used to replace the single-stage amplifier in Fig. 2.13. Fig. 2.21 and 42 show the comparison of magnitude of S_{11} for these two cases separately. As seen from Figs. 2.21 and 2.22, Wavenology EM successfully simulated the hybrid field-circuit problem with the multi-stage microwave FET amplifier embedded in the gap of a microstrip line.

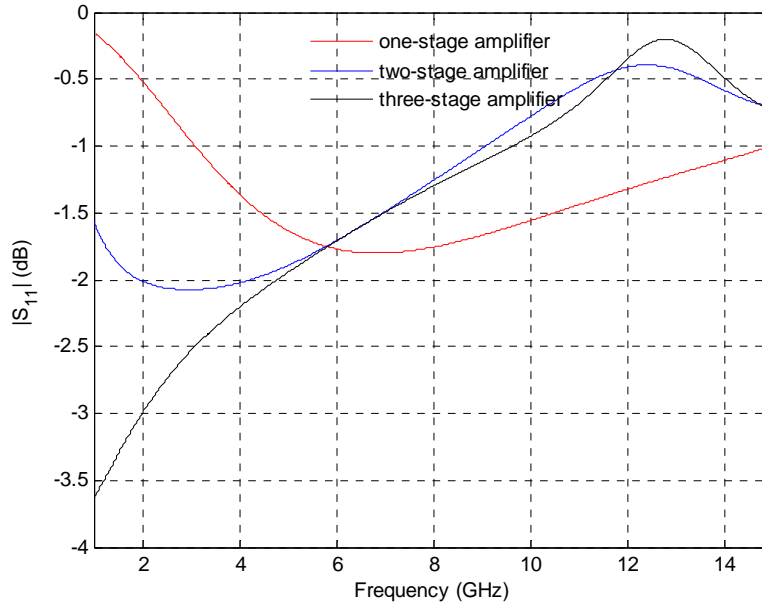


Fig. 2.21: Magnitude of the S_{11} of the amplifier circuit with one, two, and three stages in Fig. 2.13.

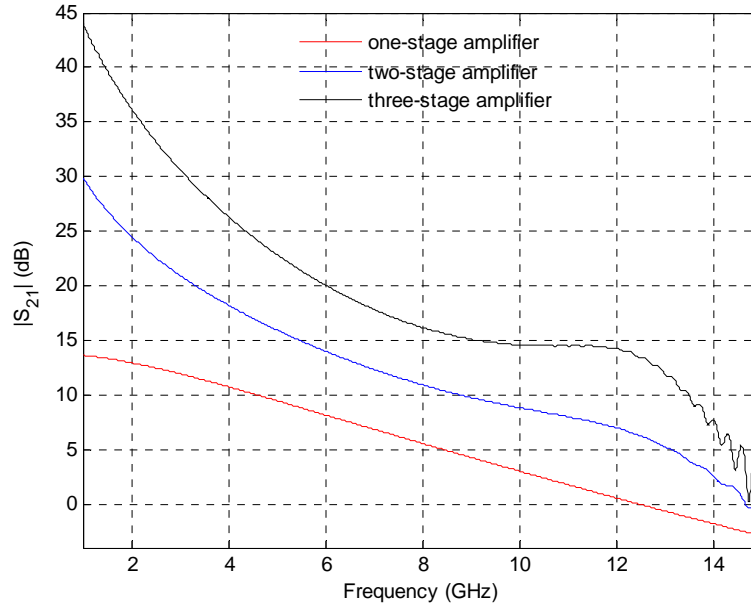


Fig. 2.22: Magnitude of the S21 of the amplifier circuit with one, two, and three stages in Fig. 2.13.

2.6. Hybrid SETD/FETD/ECT Method

2.6.1. Motivation to integrate the ECT method into the hybrid method

To apply this hybrid method, the whole computational domain is divided into a number of sub-domains according to their electrical scale properties. The SETD method is assigned to electrically large sub-domains; while the FETD method to electrically small sub-domains with fine structures. To increase the capability of the hybrid method in dealing with more complex multiscale field/circuit problems, we now further combine it with the enlarged cell technique (ECT). The ECT method is an improved conformal FDTD method which does not require a time step reduction caused by the small irregular cells around metallic boundaries. The ECT method is well suited to model electrically intermediate sub-domains because of the efficiency in the FDTD method. Another reason to add the ECT method in our hybrid method is that the circuit components can be easily and efficiently implemented and embedded in the FDTD method. Therefore, one major part of this work during this reporting period is to incorporate the ECT with our SETD/FETD method.

2.6.2. Hybridization of SETD and ECT Methods

Although the idea of hybridization is simple, to build a robust algorithm that is stable and

accurate is quite challenging because of the different characteristics of different methods. In our extensive research, we found that being free of spurious solutions is one of the most important prerequisites for the hybrid method. To achieve this goal, a one-cell layer of buffer zone of an FETD subdomain [38] is used to bridge the two totally different methods: the SETD method and the ECT method. The idea to use the FETD buffer comes from the both closeness of the FETD with the ECT and the FETD with the SETD. In other words, the FETD method serves as an effective bridge between the ECT and SETD methods. The FETD buffer shares a one-cell layer with the ECT domain. Moreover, the E nodes in the shared layer of the FETD and the ECT are at exactly the same position. The coupling of the FETD and SETD is imposed through the discontinuous Galerkin operations. Vector basis functions are employed for both FETD and SETD to avoid spurious solutions. A schematic diagram for the hybridization of the SETD and ECT method through the FETD buffer is shown in Fig. 2.22 – 2.24.

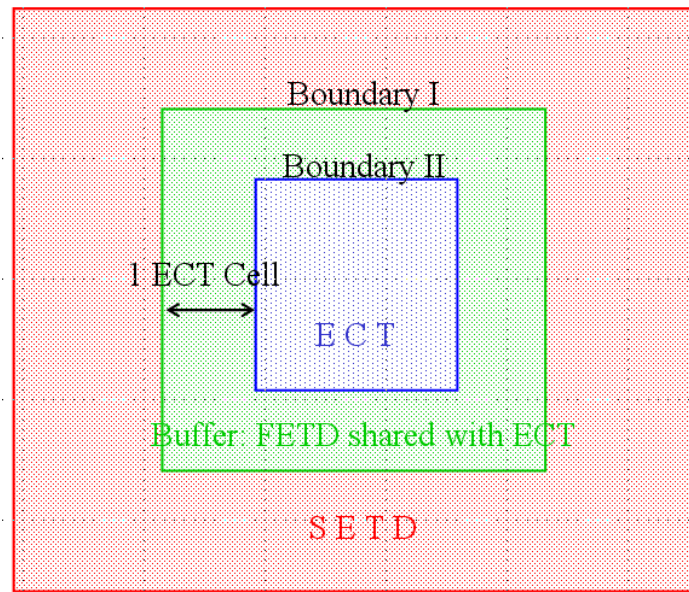


Fig. 2.22: A one-cell buffer zone of FETD is used to bridge the SETD domain and the ECT domain. The ECT domain and the FETD buffer are overlapped by one-cell layer.

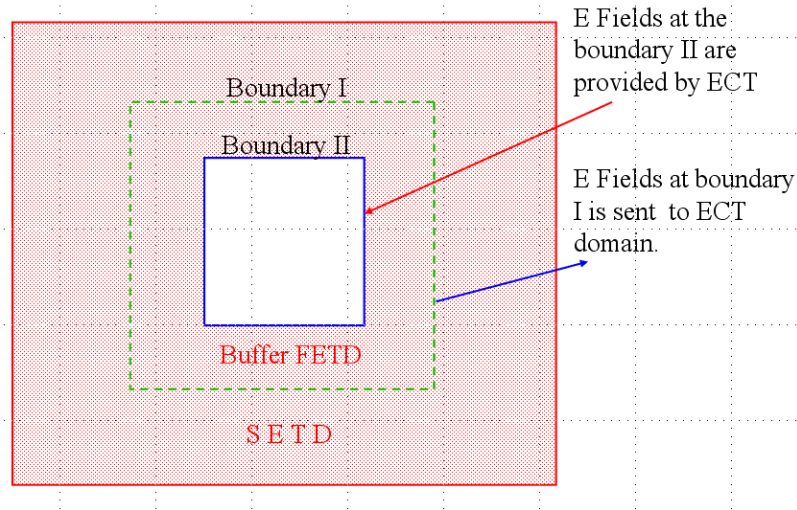


Fig. 2.23: The hybrid SETD/FETD simulation in the shaded region. After obtaining the boundary values of electric fields at boundary II from the ECT domain, the shaded region is simulated with the hybrid SETD/FETD method.

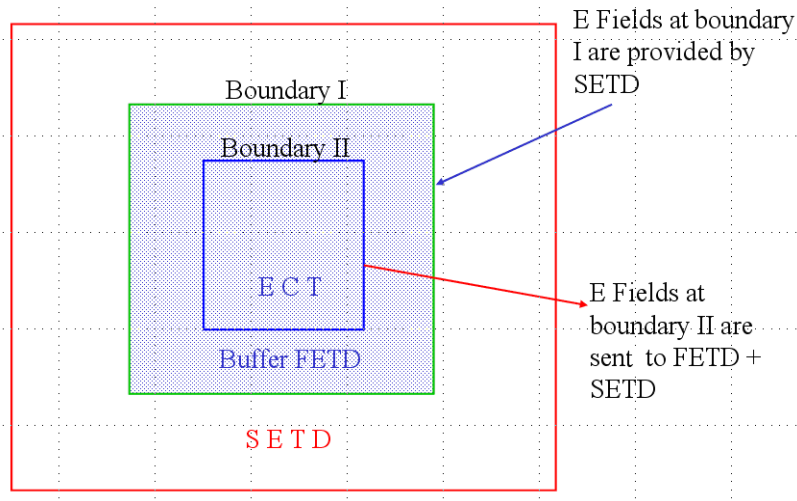


Fig. 2.24: The ECT simulation in the shaded region. After obtaining the boundary values of electric fields at boundary I from the SETD + FETD domain, the shaded region is simulated with the ECT method.

3. Parallel Computation by Multiple Threads

The simulation method we used is a hybrid multidomain method, in which the total spatial domain is divided into a number of subdomains. Each subdomain can be assigned to a different method according to its particular geometric characteristics. Three methods are available: spectral-element time-domain (SETD) method, finite-element time-domain (FETD) method, and enlarged cell technique (ECT, an improved conformal FDTD method). The multidomain method is well suited to parallel computation. We have implemented the parallel computing for the multidomain method on a shared memory computing system with multiple CPU cores, in which the updating of the fields of the subdomains is assigned to a number of cores by using multithread technique. This section introduces our parallel implementation for the hybrid multidomain method in 3 aspects: the multidomain parallelization, the multidomain balance, and the performance speedup.

3.1. Introduction of Parallelization

We introduce the parallel computation and some important issues in our designing of the parallel program for the joint field-circuit solver. For parallel computing, there are 4 types of parallelism. According to the grain, from coarse to fine, they are:

- 1. Task parallelism** – divides the problem task into several subtasks and execute them

simultaneously. In this situation, the tasks sometimes need to exchange data. Therefore, a task manager is required to synchronize the tasks.

2. Data parallelism – separates the independent data into groups, then executes them simultaneously. In this parallelism, the processing unit can be a computing node, a CPU core or the multiplier in CPU.

3. Instruction parallelism – reorders the instructions and makes them capable of executing simultaneously through a processor instruction pipeline.

4. Bit parallelism – how many bits can be executed simultaneously, for example, 32-bit or 64-bit system.

Item 4 above is hardware bus bit-width. Item 3 depends on the processor architecture and the compiler ability. Item 2 depends on the computing algorithm and the compiler ability. Item 1 depends on how to divide the algorithm into subtasks, and how to execute and synchronize subtasks on different computing nodes simultaneously. Currently, we are only interested in the parallelism in items 1 and 2.

For the task parallelism, it can be further divided into two different groups as follows according to the implementation method.

1. Multiple-threads on multiple-cores in a single computer, in which each subtask is a thread. The subtasks are executed on different CPU of the computer. This is the shared memory architecture. The balance of CPU and memory are controlled by the operating system (OS).
2. Distributed computing, in which each subtask will be sent to a core (local or remote) and executed. The progresses of those subtasks (or pass data back) are reported to a controller. The balance of program is controlled by the algorithm designer.

We have implemented the parallelism method by multiple-threads on multiple cores. The procedure of our implementation is as follows. Firstly, the computational domain will be split into several sub-domains. Then N threads are created. All the threads are managed by a thread pool, as shown in Fig. 3.1, there are 4 subdomains and 4 threads (N=4).

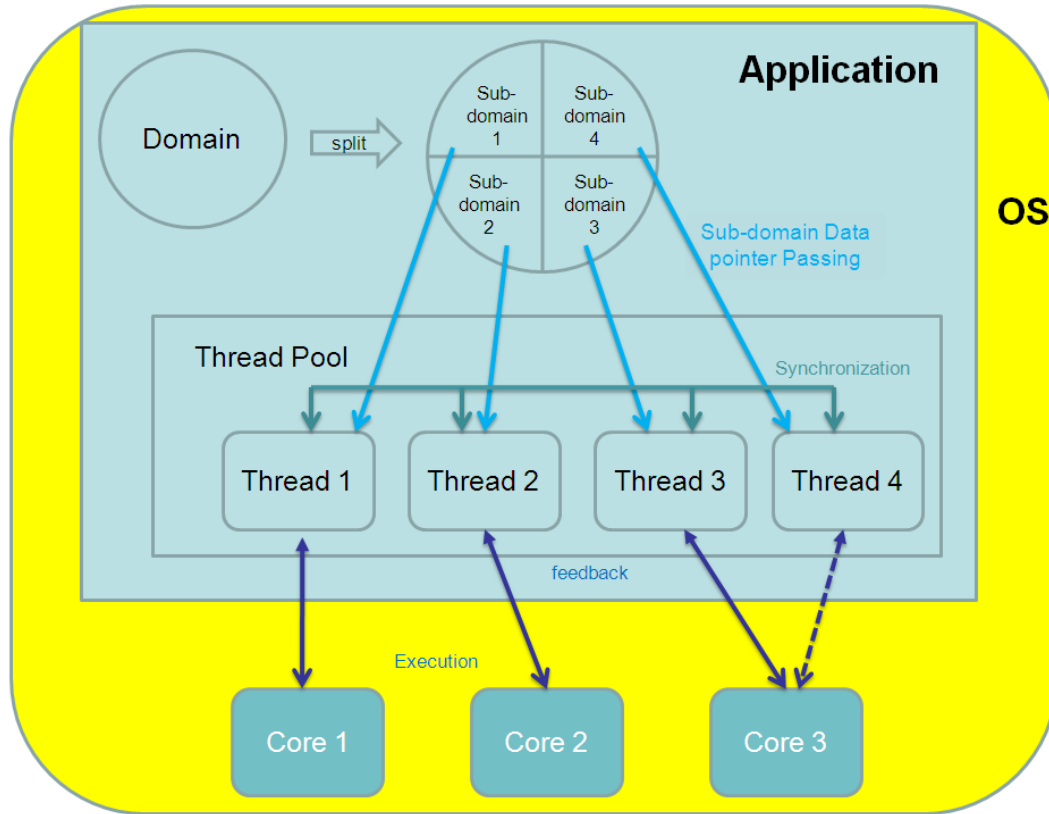


Fig. 3.1: A parallelism structure by using the multi-domain hybrid method.

At every time step in the joint field-circuit solver, we execute each thread, i.e., update the sub-domain, by one step. The maximum working (running simultaneously) thread number is decided by the maximum value between the user-defined core number and computer core number. When a thread finishes, it reports to the thread pool and pauses to let thread pool start a waiting thread. After all threads finish, the thread pool will exchange data among all threads and record data, and additionally, report to application if necessary. Then all threads resume to the next step.

3.2. Multidomain Parallelization

We implement the parallel method for our hybrid solver on a shared memory machine with multiple cores using multithread technique. With user suggested number of multiple-threads, we will create N threads ($N = \min(M, \min(O, P))$, where M is the number of subdomains, O the number of user suggested threads, and P the number of available CPU cores). Using this formulation, we can limit that there is only one thread running on one core at most; and eliminate the time on thread switching to increase the performance. For each thread, we will assign some subdomains, depending on how we balance the tasks on each thread, into each thread's job-list. There are 3 types of solvers for current hybrid method, FDTD, FETD and SETD. Each sub-domain

can be solved by any one of these 3 solvers. Here, we illustrate how to parallelize one case with nine sub-domains, which has 3 FDTD sub-domains, 3 FETD sub-domains and 3 SETD subdomains.

FDTD	FDTD	FDTD
FETD	FETD	FETD
SETD	SETD	SETD

Fig. 3.2: A computational domain with 3 FDTD subdomains, 3 FETD subdomains and 3 SETD sub-domains.

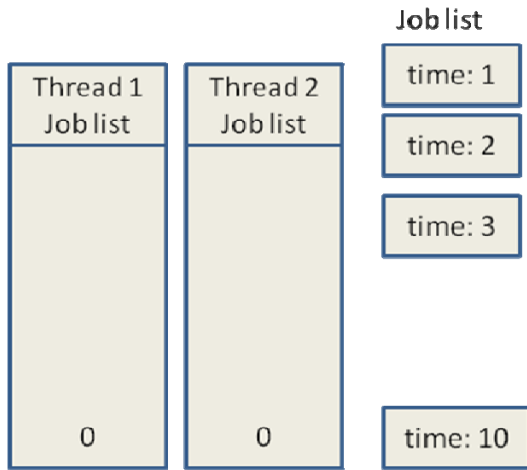
We assume 3 threads will be used in the simulation for the case in Fig 3.2. We will assign one FDTD, one FETD and one SETD subdomain for each thread. The general scheme for the parallel computing of the hybrid multidomain method is as followed. At first, we update FDTD sub-domains simultaneously. Then pass the EM field from FDTD sub-domains to adjacent FETD or SETD sub-domains. Next, we update FETD sub-domains or SETD sub-domains simultaneously (the running sequence of FETD and SETD solver can be arbitrary) and exchange EM field between FETD sub-domains or SETD sub-domains. Finally, we need to pass EM field from FETD sub-domains or SETD sub-domains to FDTD sub-domain.

3.3. Multidomain Balance

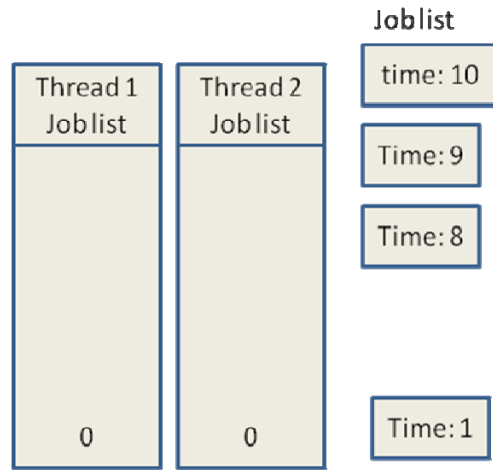
In general, different domain has different number of unknowns, and even for the same number of unknowns, different solver requires different solving time. Moreover, sometimes the number of subdomains is much larger than the number of threads. Waiting time among different threads is necessary to ensure all the subdomains are updated in the same pace. To reduce the waiting time, we balance the load on each thread to let them be able to finish approximately at the same time. In the load balance method, we roughly assume that the subdomain solving time is proportional to the number of unknown in the subdomain. An example is given as follows.

Assume that 2 threads need to balance and the computational load is 10 subdomains whose solving

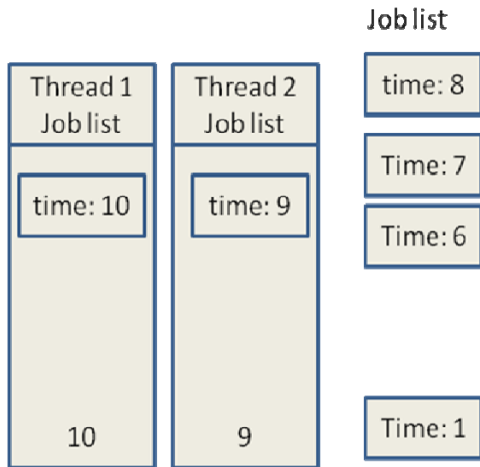
times are evaluated as 1 to 10. As shown in Fig. 3.3, we firstly reorder the load to a list with a descending order. Then we assign the first load of the list to a minimal running time thread, remove the load from list, and sum the thread running time as the loads assigned to it. We repeat this assign-remove-resume procedure until the job list becomes empty. It can be seen in Fig. 3.3 that the final running time of two threads is 28 and 27, which means that the load is almost evenly assigned to the threads.



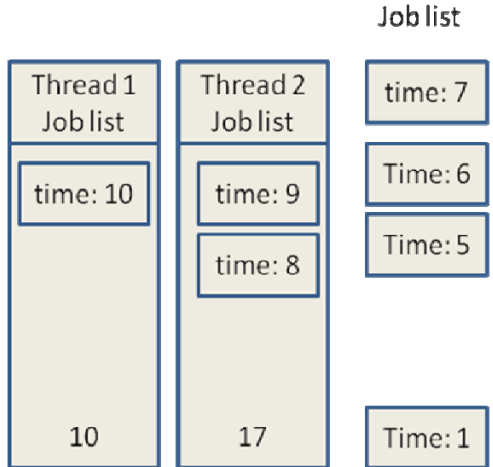
(a) Original state



(b) Sort Job list



(c) After 2 assign-remove-resumes.



(d) After 3 assign-remove-resumes

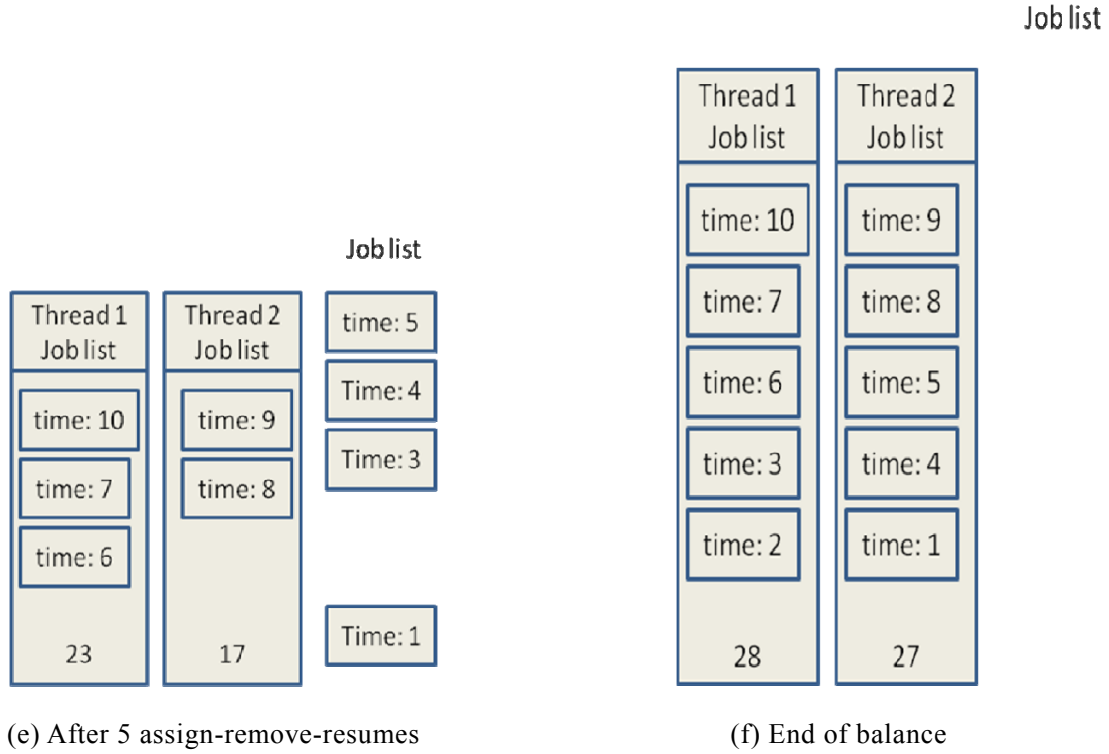


Fig 3.3: Balance 10 subdomains on 2 threads.

3.4. Performance Speedup

An example is used to test the performance speedup of the parallel computation. As shown in Fig. 3.4, a multidomain with 56 SETD, 3 FETD and 1 FDTD sub-domains is studied. We evaluate the performance speedup with 1, 2, 3 and 4 threads respectively.

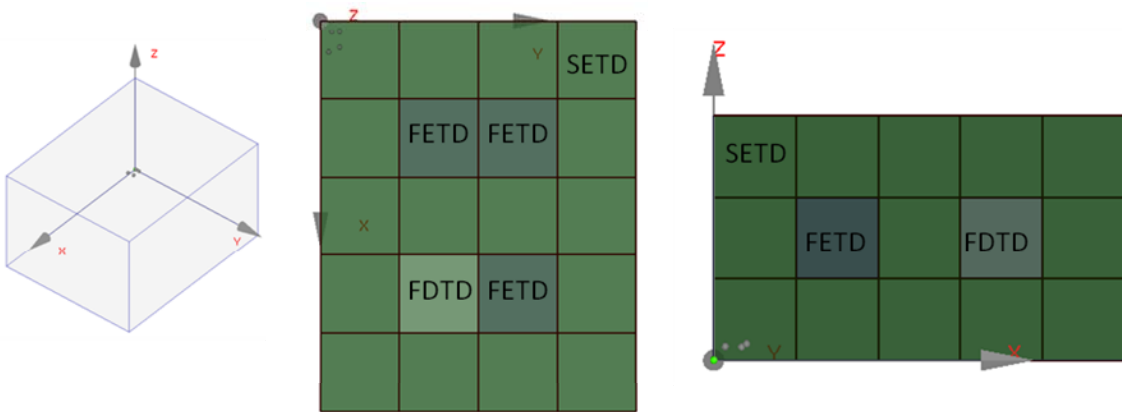


Fig. 3.4: An example of multidomain with 56 SETD, 3 FETD and 1 FDTD subdomains.

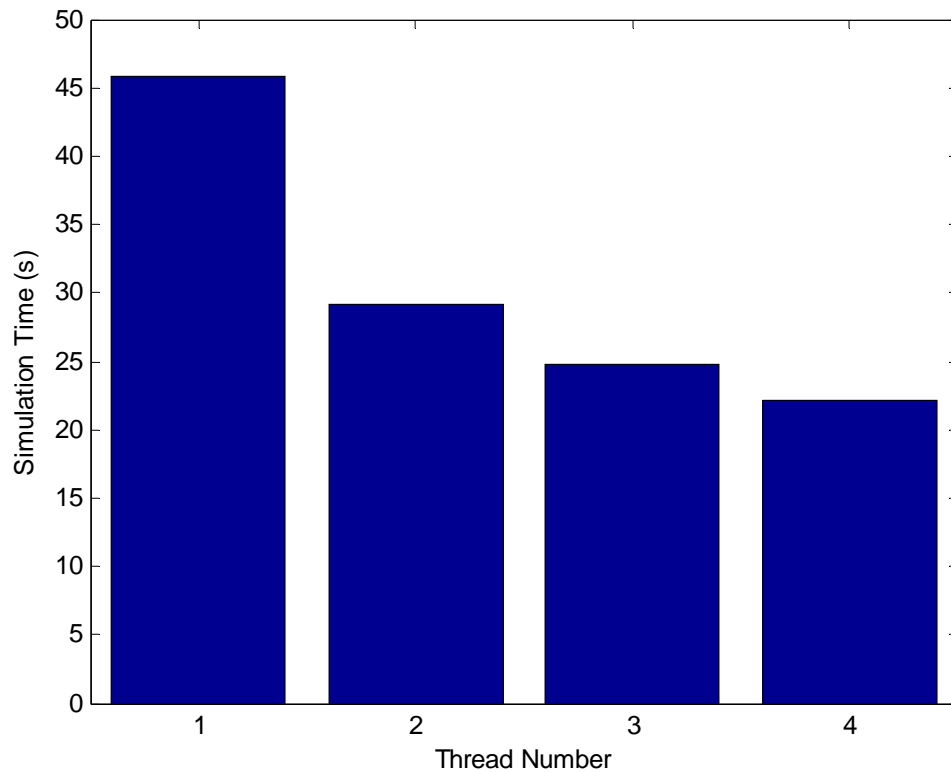


Fig. 3.5: Simulation time with different number of threads for the example in Fig. 3.4.

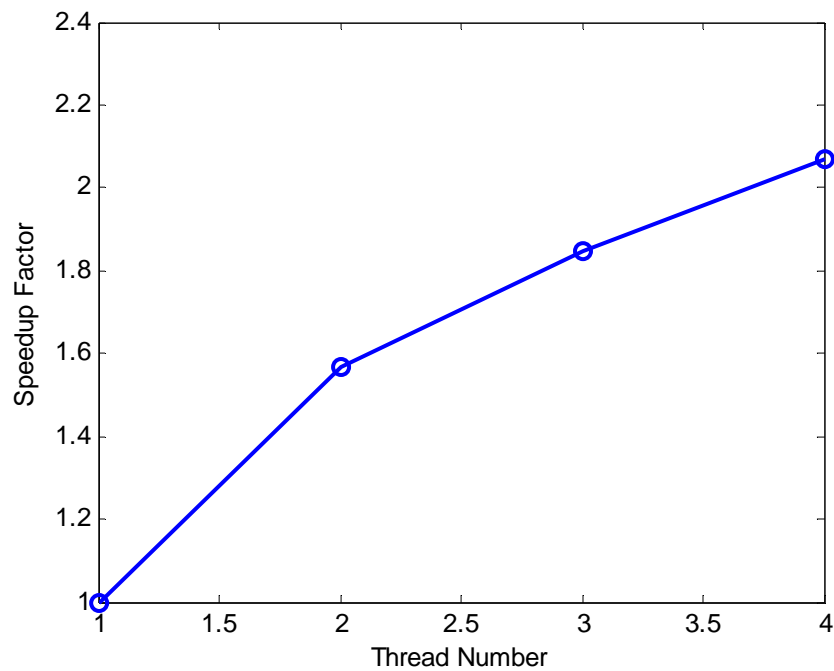


Fig. 3.6: Performance speedup factor of parallel computation for different number of threads.

The speedup factor is shown as Fig 3.6 where the speedup factor is not ideally linear with the thread number. They are two reasons. The first is that we need to run FDTD domain firstly, then run FETD and SETD domain because of the different time integration methods between the FDTD and FETD/SETD methods. The second is come from the hardware limitation. We use a computer with Intel Q6600 CPU and 4 GB DDR2-800 memories. The memory bandwidth limits the system speedup. A similar phenomenon has been also observed in our parallelized FDTD method.

3.5. Numerical Results

To verify the hybrid method using the parallel algorithm, a homogeneous rectangular cavity model, which includes a SETD domain, a FETD domain, and ECT domains, is presented as shown in Fig. 3.7. This cavity has a dimension of 2.5 m x 2 m x 1.5 m and has 5 x 4 x 3 subdomains. A dipole source with the maximum frequency of 100 MHz is at (0.2, 0.2, 0.2) m and an observer is located at (1.2, 1.1, 0.8) m. The computed electric field at the observer is compared with that by using a pure FDTD method with 40 PPW, as shown in Fig. 3.8, where a good agreement is obtained. The CPU time of this cavity is 110 s by 1 core, 85 s by 2 cores, 59 s by 3 cores, and 57 s by 4 cores.

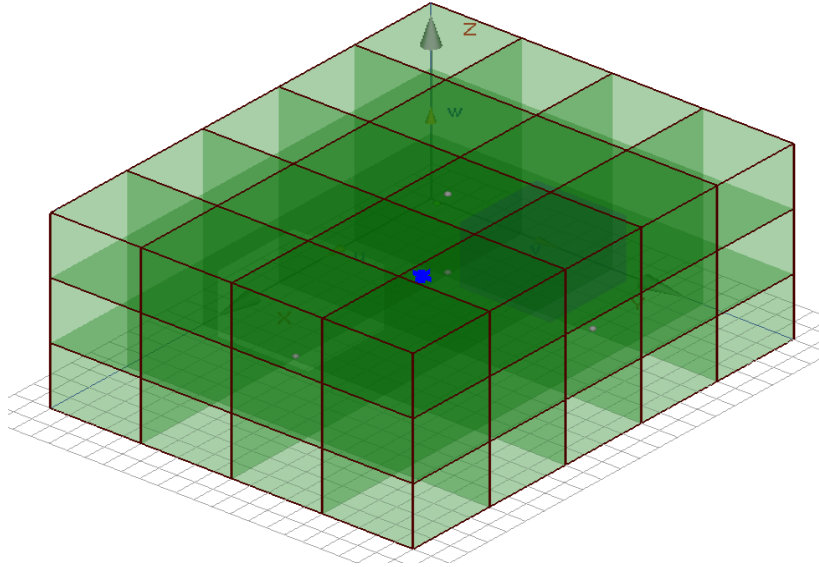


Fig. 3.7: Rectangular cavity model. Lower corner is (0, 0, 0) m and upper corner is (2.5, 2.5, 2). SETD domain is located at [4, 2, 2], FETD domain at [2, 3, 2], and the others are FDTD domains.

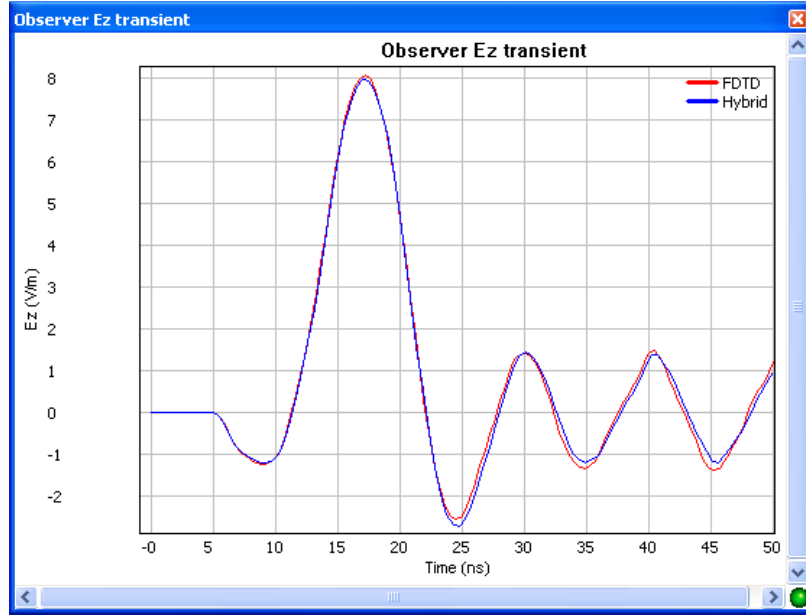


Fig. 3.8: Comparison of electric field at (1.2, 1.1, 0.8) m.

The second example is an inhomogeneous case with a curved geometry. As shown in Fig. 3.9, a ring structure has a dielectric constant of 9.8. A BHW plane wave propagating in (45, 45) degree is incident and an observer is put at (150, 0, 20) mm. The ring structure is discretized by a tetrahedron mesh and FETD method is applied at this subdomain. To validate the results, the electric field at the observer is compared with that by using pure FDTD method with a high sampling density. The comparison is shown in Fig. 3.10, where a good agreement is obtained. The CPU time is 2394 s by using 1 core, 1496 s by using 2 cores, 1271 s by using 3 cores, and 1199 s by using 4 cores.

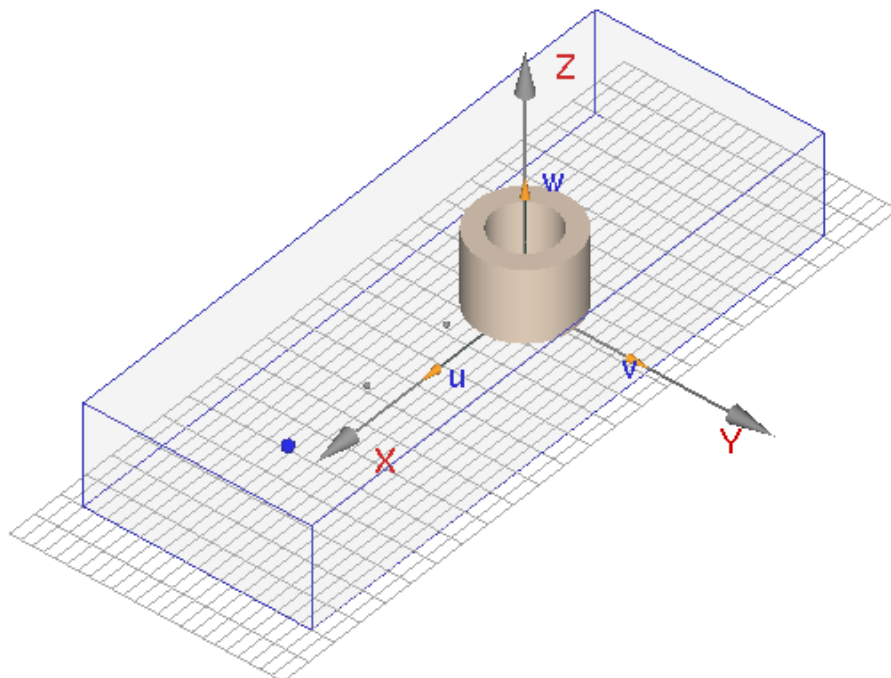


Fig. 3.9: A dielectric ring model. The ring's height is 39 mm, inner radius is 16.54 mm, and outer radius is 26.75 mm.

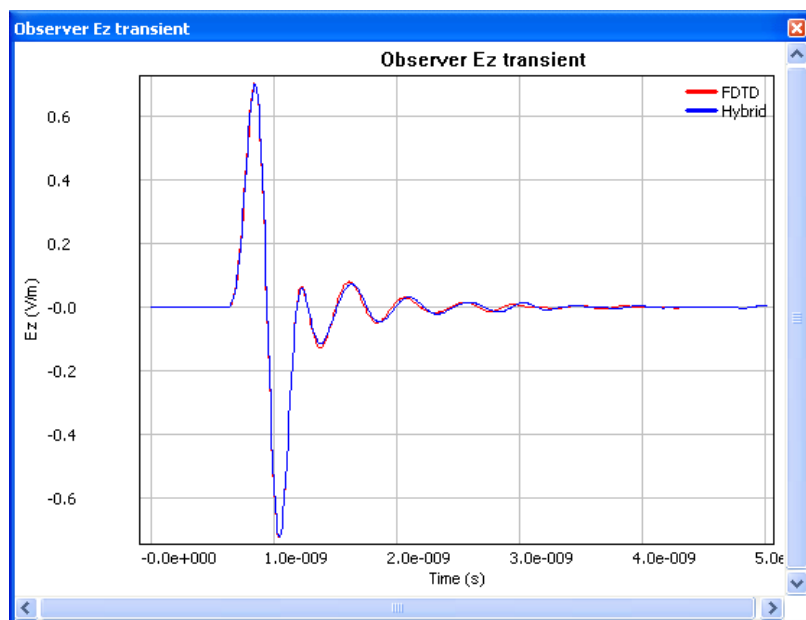


Fig. 3.10: Comparison of electric fields at the observer by hybrid method and pure FDTD.

4. PARALLEL COMPUTATION by GPU

Up to date, General-Purpose computation on Graphics Processing Units (GPGPU) is becoming a popular technology to speed up the task with high computational density. The basic idea is that the multiple identical execution cores in a Graphics Processing Unit (GPU) can execute the instructions in parallel. If a task can be divided into multiple sub-tasks, each sub-task can be individually delivered to a GPU execution core and then all sub-tasks can be executed in parallel. Thus, the total time cost for this task will be reduced. For an FDTD method, due to the localization of the memory and operations, it can fully take advantage of this kind of parallelization and obtain very high speed up.

4.1. Platforms

There are several types of GPGPU platforms and programming languages available. The most direct development platforms come from the GPU manufactures. The NVidia Corp. creates the Cuda platform based on their GPU; and the AMD Corp. creates the Stream platform based on their GPU. These two platforms cannot work cross-platform. Microsoft also released their GPGPU API in Directx11; it is compatible with NVidia's GPU and AMD's GPU. The highest level programming platform is OpenCL (Open Computing Language). It is a framework for writing programs that execute across heterogeneous platforms consisting of CPUs, GPUs, and other processors. Currently, NVidia, AMD and Microsoft all provide API to port their private GPGPU API to OpenCL.

All these development platforms have their advantages and disadvantages. For Cuda, it can develop fastest codes today, but it can only work on the NVidia's hardware. For Stream, the performance is less than Cuda. The performance of GPGPU API in Direct11 is the slowest one compared with Cuda and Stream, but it has more compatible capability. The OpenCL has the best compatible capability among these platforms. But the standard of OpenCL is just established last year, and there are not enough documentations and programming references on it.

By comparing all the available techniques, we choose NVidia's Cuda development platform as our GPGPU speedup engine.

4.2. GPU acceleration method on CUDA Engine

In ECT (a boundary conformal FDTD method), the updating scheme of the electric field depends only on the field itself and adjacent magnetic fields. Therefore, all electric field components can be updated in parallel if a system has independent memory for electric field and

the magnetic field components. Similarly, the magnetic field components have the same property. Thus, it makes the FDTD method ideal for GPU acceleration. We have implemented GPU acceleration based on the Nvidia CUDA engine. This section introduces our acceleration method in two aspects: the GPU acceleration method and the performance.

In CUDA engine, a parallel code can be run on a grid with $A \times B$ blocks. Each block has $C \times D$ parallel threads. For a graphic card with M CUDA cores, we can make $C \times D \times K = M$, where $K = [2^n \dots 2^n]$ and n and M are integer numbers. Therefore, a parallel code can be finished on the grid by $A \times B / K$ runs. For a typical middle-end Nvidia GPU, for example, 9600 GSO, the number of CUDA cores can be around 100. Thus, a parallel code on CUDA engine can obtain significantly speedup. For the electric and magnetic fields in an FDTD computation domain, they are organized as $N = x \times y \times z$ cells. In our parallelized GPU code, we organized CUDA cores by a grid with $\text{ceil}(x/12) \times \text{ceil}(y/8)$ blocks and each block has $12 \times 8 = 96$ threads. For each thread, it will update the field along z axis only. Therefore, our code has approximate $(96/M) / \text{ceil}(96/M) \times M$ parallelization in field updating.

Fig. 4.1 shows the flow chart of the GPU acceleration implementation in our FDTD solver. Another consideration is the effect of the data transfer between the computer system memory and GPU local memory. The data transfer includes the source excitation and field fetching. The CUDA code can only run on a GPU and operate on the GPU local memory. For a realistic EM simulator, it is necessary to add source excitation on the fields at each EM updating time step. CUDA core is designed for simple calculation and the CUDA engine can only support limited math functions. But the excitation pulse in Wavenology EM package supports a combination of complicated math functions, some of them are not supported by CUDA engine. Therefore, the excitation at each time step must be calculated serially on CPU and then transferred to GPU, thus decreasing the speedup performance. In addition, Wavenology EM package needs to record the EM field at every step or at every several steps. As mentioned above, the fields are stored in GPU memory only. Thus, data transfer from GPU memory to system memory is required also. Due to the fact that the data transfer speed between system memory is much slow than regular CPU-system memory transfer speed, it will decrease the speedup performance also. Because of these two factors, the speedup factor of the GPU implementation will be understandably lower than the number of threads; nevertheless, our performance study below shows that the speedup is quite good.

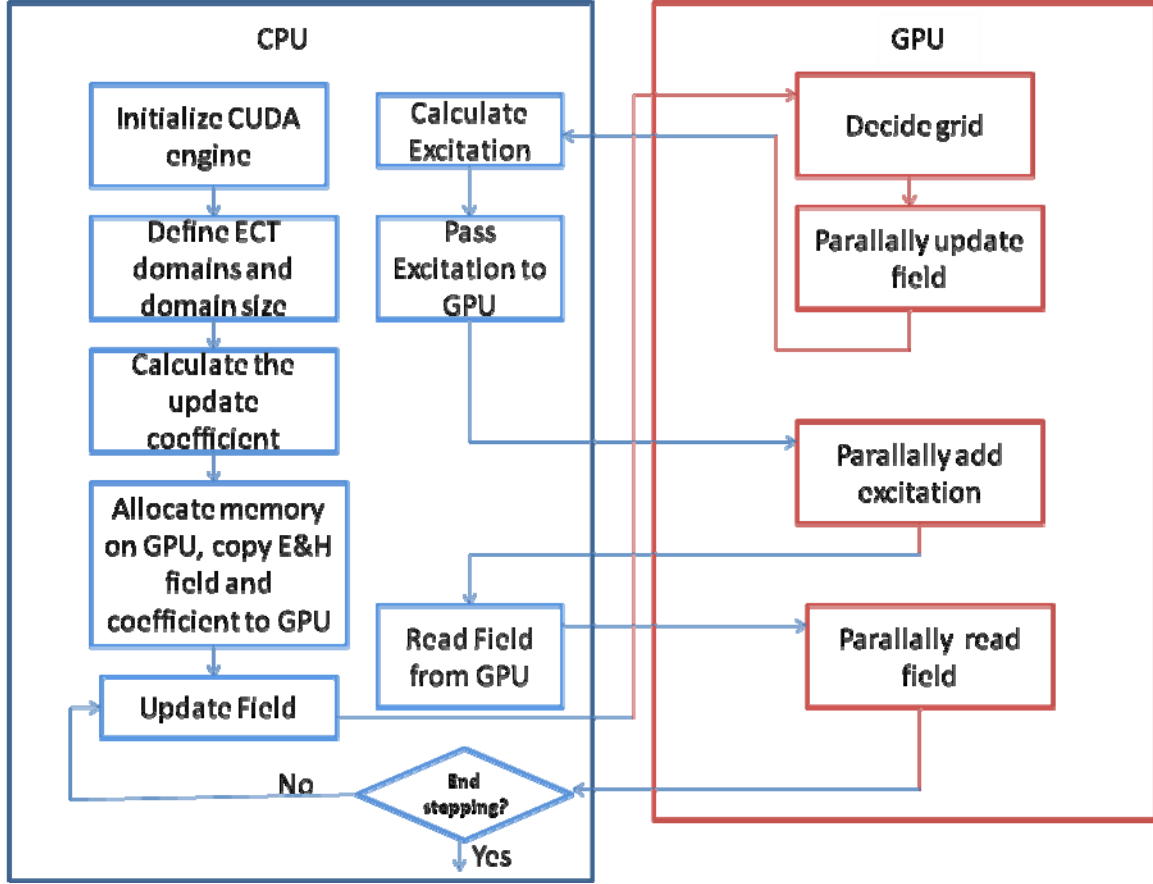


Fig. 4.1: The flow chart of the GUP acceleration implementation in FDTD method.

4.3. GPU Acceleration Examples

We show the performance of the GPU acceleration in Wavenology EM package. In the simulation, we use an Nvidia 9600GSO graphic card, which has 384 MB local memory, and 96 CUDA cores. The maximum number of threads that can be created on GPU is 65535 and the maximum number of threads in each block is 512. The CPU core clock is 1375 MHz and the GPU memory clock is 800 MHz. The CPU system has a 4-core CPU Intel Q6600 with DDR2-800 memory. As mentioned above, in our current implementation, we fix the GPU block as 12×8 threads per block. We use a single domain cavity case to compare with a benchmark case: the Nvidia CUDA example FDTD3D. This example implements a finite-differential-time-domain method on single field propagation in a 3D space. We consider a cavity model which includes two electric dipole sources and three observers to record the signal. The computation domain is divided into $100 \times 100 \times 100$ and $280 \times 280 \times 16$ cells, respectively. The fields are recorded at every time step.

The speedup performances for the cavity cases and CUDA example FDTD3D are shown in the Table 4.1.

Table 4.1: The speedup performance comparison

Case Name	FDTD cavity 100×100×100 cells	FDTD cavity 280×280×16 cells	Nvidia CUDA example FDTD3D 280×280×280 cells
Speedup factor	20.2	22.4	40.1

As shown in the table 4.1, the GPU speedup factor in the FDTD solver of Wavenology EM is about 20, while the CUDA example FDTD3D is 40. It is reasonable because of the following aspects:

1. Example FDTD3D does not have a source which needs to be calculated in the CPU and then transfer to GPU.
2. Example FDTD3D does not need to read field from GPU at every time step.
3. Updating of the FDTD is more complicated than the example FDTD3D. The FDTD needs to update 6 field values by 21 memory locations, while the FDTD3D only needs to update one field by 6 memory locations.

Table 4.1 also shows that larger $x \times y$ case has better speedup performance in our implementation: the second case with 280×280×16 cells has a speedup factor of 22.4, while the first case with 100×100×100 cells has a speedup factor of 20.2.

4.4. Implementation of PML subdomain

As we demonstrated the performance of the GPU acceleration for cavity cases with electrical dipole sources and observers. We found there are two factors that affect the performance of the GPU acceleration. One is the data transfer between the GPU and the system main memory. Another is the mesh size in XY plane. In this period, we have evaluated the effect of additional PML sub-domains for the GPU acceleration. PML, which is a sub-domains as absorbing boundaries, has 10 layers in its direction.

Due to 10 layers for each PML sub-domain, those 4 small subdomains of PMLs have 10 x 10 x 10 cells, which do not match our GPU block size (12 x 8 in XY plane), and thus limits the performance. Fig. 4.2 shows the flow chart for time stepping in the GPU acceleration. The PML is implemented separately in 26 subdomains. The performance of whole stepping is affected by the performance of each sub domains. Therefore, the small PML sub domains will decrease the GPU

acceleration performance.

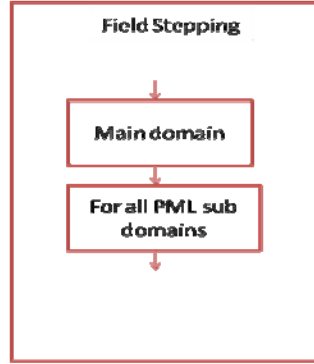


Fig. 4.2: Flow chart of sequential time-stepping of domains.

We found that our implementation on the GPU acceleration requires a modification in the stepping scheme to reduce the impact of data transfers between the GPU and the CPU system main memory. It is possible to take advantage of multiple-streams technology in CUDA to step PML subdomains in parallel to reduce the time in PML stepping, as shown in Fig. 4.3.

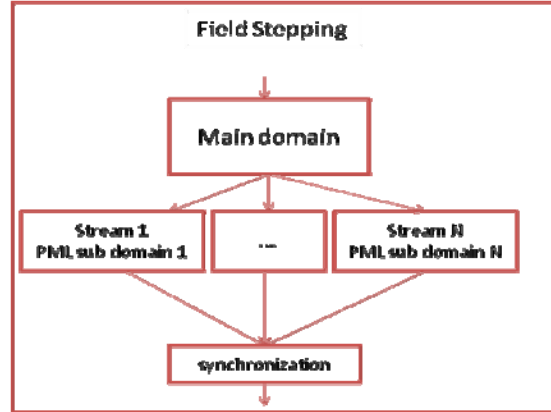


Fig. 4.3: Flow chart of time stepping for multiple-streams domain.

4.5. Examples of PML subdomain

This first example is a $50\ \Omega$ strip line which is composed of a PEC ground, a RT Duroid substrate ($\epsilon_r=2.2$, thickness 0.794 mm) and a PEC patch with width of 2.413 mm as shown in Fig. 4.3. A lumped port (I) is connected to a terminal of strip line as an excitation. A $50\ \Omega$ resistor (RI) is attached at the other terminal of strip line as a load. The boundary conditions of this case are

PML except z_{\min} position where PEC boundary condition is applied.

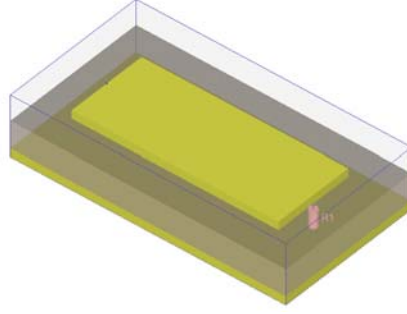


Fig. 4.3: Configuration of the strip line.

Due to the fact that there are only one source and one data point to be recorded in this example, the data transfer between the GPU and the CPU system main memory is minimized. Therefore, the performance of GPU speedup will be dominated by the mesh size in XY plane and the PML sub-domains. We use different mesh resolutions to evaluate the performance of the GPU acceleration. The GPU speedup factor is defined as the ratio between the CPU time in the serial code and that in the GPU accelerated code. The result of speedup factor for this example is shown in table 4.2. We achieve a factor of 12.1 speedup using the GPU for this example when the number of cells is $100 \times 100 \times 80$.

Table 4.2: Comparison of speedup performance for the strip line case

Main Computation Domain Mesh size	$8 \times 12 \times 12$ cells	$30 \times 30 \times 30$ cells	$100 \times 100 \times 80$ cells
Speedup factor	0.7	5.2	12.1

From the table 4.2, the performance of the GPU code is better as the size of mesh increases. The speedup factor of the Cavity case is about 20, while the strip line is only about 12. The main reason for this is the usage of PML sub-domains. In our GPU code, we step all domains sequentially. Therefore, a one-domain with small mesh size can impact the performance of the whole code.

The second example is an ultra wideband antenna which is fed by a lumped port (I) and is working in an open space as shown in Fig. 4.5. We put several observers to record near fields. All boundary conditions of this case are PML and thus this model includes a main domain and 26 PML sub-domains.

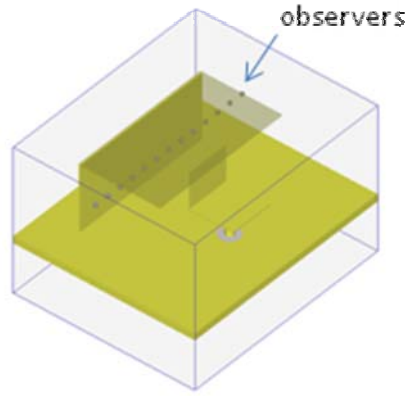


Fig. 4.5: Configuration of the ultra wideband antenna.

Due to more data transfers between the GPU and the CPU system main memory and more PML sub-domains, the performance of GPU speedup will be lower than the strip line case. Here, we use different mesh resolution and different number of observers to evaluate the performance of the GPU acceleration. The resultant speedup is shown in the table 4.3.

Table 4.3: Comparison of speedup performance for the wideband antenna

Main Computation Domain Mesh size	$51 \times 72 \times 54$ cells 13 observers	$104 \times 102 \times 78$ cells 5 observers	$104 \times 102 \times 78$ cells 13 observers
Speedup factor	8.9	10.4	9.7

The GPU speedup is about 10. Due to the large of XY mesh we can get better performance. But the number of data transfers between the GPU and the system main memory will decrease the speedup performance.

5. COMPREHENSIVE TESTINGS

Our field/circuit software package combines three efficient electromagnetic field algorithms, the SETD for coarse scales, the ECT (an improved conformal FDTD method) for intermediate scales, and the FETD for fine scales, together with nonlinear circuit solvers (both SPICE circuit solver and our internal circuit solver) to solve complex multiscale problems. A number of cases are tested to verify and validate the accuracy and efficiency of our field/circuit software package.

5.1. Plane Wave Incident on a Large Domain

- **Purpose:** Verify the high accuracy and efficiency of the DG-SETD method in simulating large-scale problems.
- **Model:** The geometry of the case has a large dimension of 10 wavelengths along all the three Cartesian directions. A simple homogeneous model with a plane wave incidence is employed to examine the accuracy of the numerical results, since the analytical solution for such a model is known.
- **Result:** DG-SETD is much efficient than FDTD in both required memory and CPU time as shown in Table 5.1 and Table 52.

Table 5.1: Comparison between DG-SETD and FDTD at 1% error tolerance

	Mesh Size	Memory (MB)	CPU Time (s)
FDTD	300 x 300 x 300	3,844	1,522
DG-SETD	63 x 63 x 63	270	683
Gain Ratio by DG	108	14.2	2.2

Table 5.2: Comparison between DG-SETD and FDTD at 0.1% error tolerance

	Mesh Size	Memory (MB)	CPU Time (s)
FDTD	600 x 600 x 600	20,656	18,309
DG-SETD	77 x 77 x 77	380	2,297
Gain Ratio by DG	473	53.3	8.0

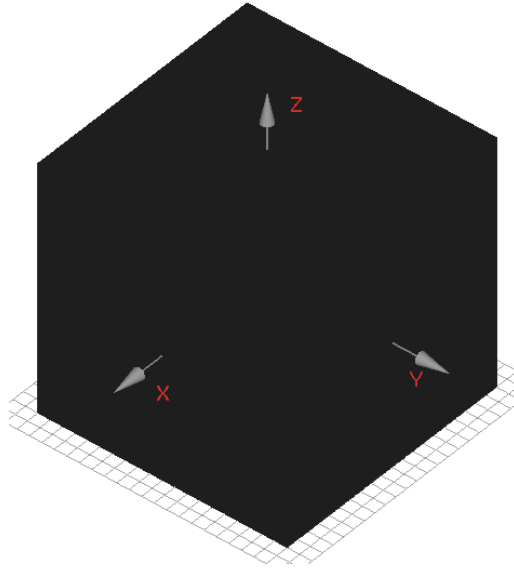


Fig. 5.1: The mesh of the FDTD method for the 10 x 10 x 10 wavelength problem. It has 300 cells in each direction, requiring 30 points per wavelength to get 99% accuracy (1% error).

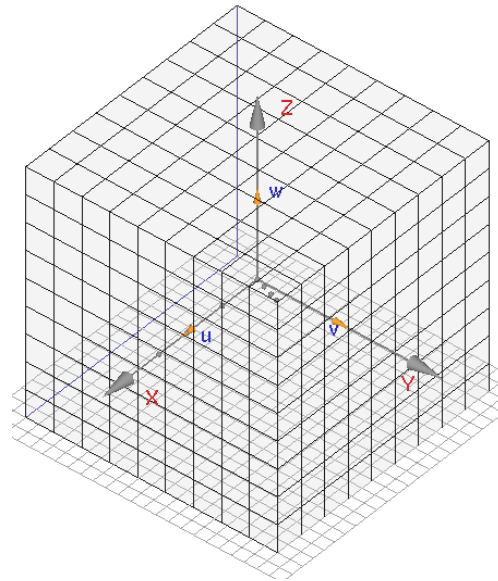


Fig. 5.2: The mesh of the DG-SETD method for the 10 x 10 x 10 wavelength problem. It has 9 elements in each direction. For each element, the 7th order SETD basis functions are used. Generally, it requires only 6.3 points per wavelength to get 99% accuracy.

5.2. Scattering of a Tilted Thin PEC Plate to an Electric Dipole Wave

- **Purpose:** Test the accuracy and performance of the hybrid code in dealing with highly fine details in an intermediate sized problem.

- **Model:** A thin tilted PEC plate oriented along (1, 1, 1) direction is used to represent the highly fine details. The thickness of the PEC plate is 3 mm, only 0.006 wavelengths relative to the maximum frequency (600 MHz). An electric dipole aligned along the z direction is placed at (250, 100, 250) mm. Three receivers are placed at the positions (250, 400, 150), (250, 800, 250), and (250, 1200, 250) mm, respectively.
- **Result:** The hybrid method is 46.4 times more efficient than the pure FDTD method in computational memory and 1.5 times faster than the FDTD method, while Good agreement is obtained with the FDTD results.

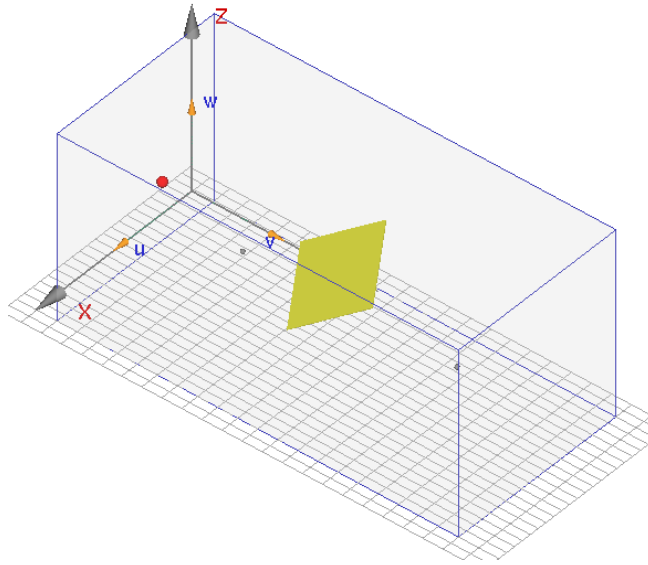


Fig. 5.3: Scattering of a Tilted Thin PEC Plate to waves generated by an Electric Dipole polarized along the z direction. The model includes: (1) a tilted thin PEC plate (yellow region) at the center; (2) an electric dipole (red dot) at the left; and (3) three receivers (grey dots), in front of, close to, and after the plate, respectively.

Table 5.3: Comparison between hybrid FETD/FDTD and FDTD method for PEC plate case

	Mesh Size	Memory (MB)	CPU Time (s)
FDTD	235 x 245 x 232	18,410	6,510
Hybrid FETD/FDTD	33 x 17 x 17 + 9,345	397	4,290
Gain Ratio by Hybrid	707	46.4	1.5

5.3. A Patch Antenna in a Reverberation Chamber

- **Purpose:** Test the accuracy and efficiency of the hybrid FETD/SETD method.
- **Model:** A patch antenna is measured in a reverberation chamber with a metallic stirrer. The ratio of the largest dimension to the smallest dimension in this case is $1.6\text{ m} / 2\text{ mm} = 800$, which means a typical multi-scale structure. The subdomains containing the antenna and the stirrer are discretized by finite elements with dense meshes (first order tetrahedral mesh with a sampling density equal to 20 PPW), and all the other subdomains are discretized by higher order spectral elements with coarse meshes (fifth order hexahedral mesh with a sampling density equal to 10 PPW).
- **Result:** Table 5.4 lists the comparison of computational costs by the two methods from which we observe that the hybrid SETD/FETD method is more efficient than the conventional FDTD method for such multiscale electromagnetic simulations.

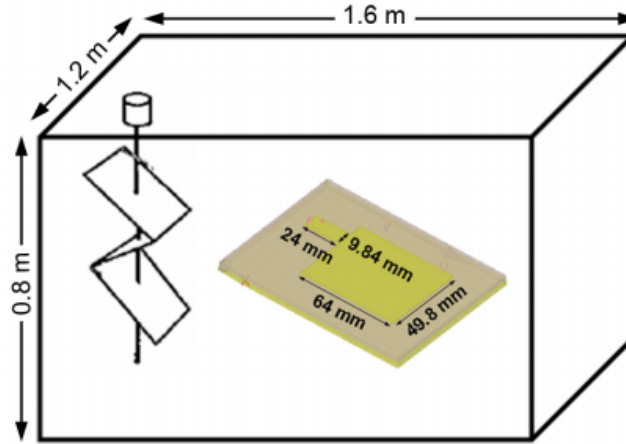


Fig. 5.4: A patch antenna measured in a reverberation chamber. The size of this chamber is 1.6 m x 1.2 m x 0.8 m. The thickness of the metallic stirrer and the patch antenna are 5 mm and 2 mm, respectively.

Table 5.4: Comparison of hybrid and FDTD method

	Memory (MB)	CPU Time (h)
FDTD	2,560	5.7
Hybrid FETD/SETD	730	4.2
Gain Ratio by Hybrid	3.5	1.4

5.4. A Tilted Parallel Wire Transmission Line Operated by Lumped Ports

- **Purpose:** Test the integration of the hybrid method with circuit elements.
- **Model:** A tilted thin parallel wire transmission line is operated by two lumped ports. One of the lumped ports is used to excite the transmission line, while the other one is used to receive the signals propagating through the transmission line. The thickness of the wires is 1 mm, about 0.0033 wavelengths with respect to the excited maximum frequency. This transmission line problem has multiple scales: the fine scales around the thin wires and the coarse scales cover the open air area. To solve the multiscale problem, a hybrid FETD/FDTD method is applied. At the center around the thin wires, an FETD subdomain is placed. Elsewhere, FDTD subdomains are placed.
- **Result:** The unstructured mesh is much more efficient in capturing arbitrarily shaped small details than the structured Cartesian mesh used by the FDTD method. It requires much fewer elements. The simulation by the hybrid method takes less than 2 hours and requires only 729 MB memory.

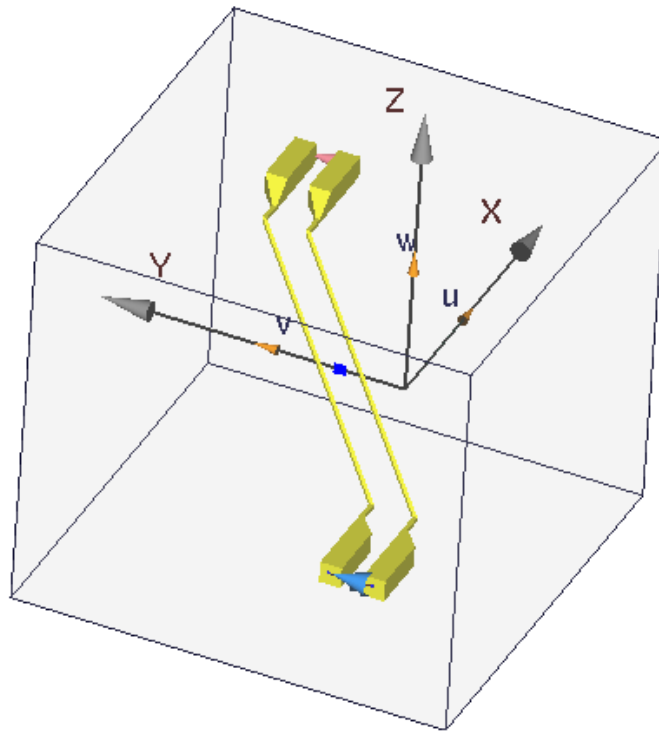


Fig. 5.5: A tilted thin parallel wire transmission line is connected to two lumped ports. The port denoted by a red arrow is used to excite the transmission line, while the port denoted by a blue arrow is used to receive the signals propagating through the transmission line.

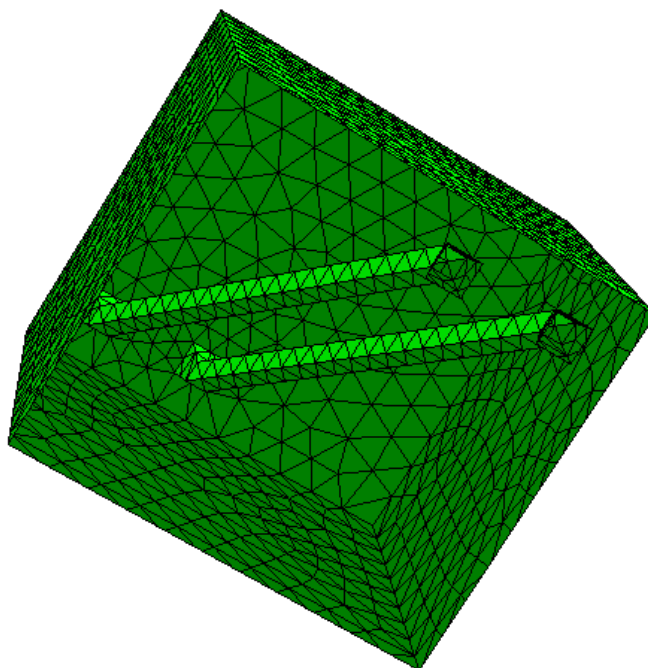


Fig. 5.6: FETD mesh for hybrid method. The number of tetrahedron is 8226 and the number of unknown is 64,597.

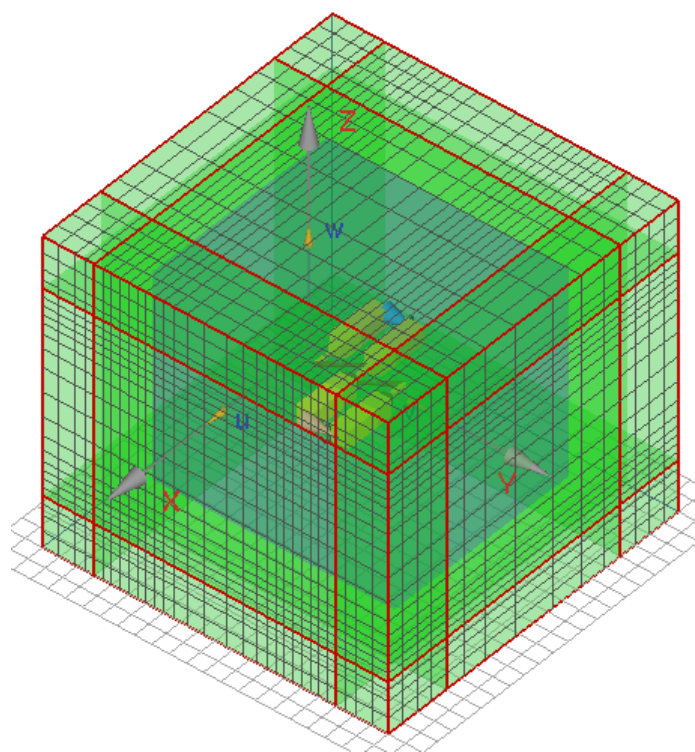


Fig. 5.7: This total domain is divided into 3 x 3 x 3 subdomains. At the center around the thin wires, an FETD subdomain is placed. Elsewhere, FDTD subdomains are placed.

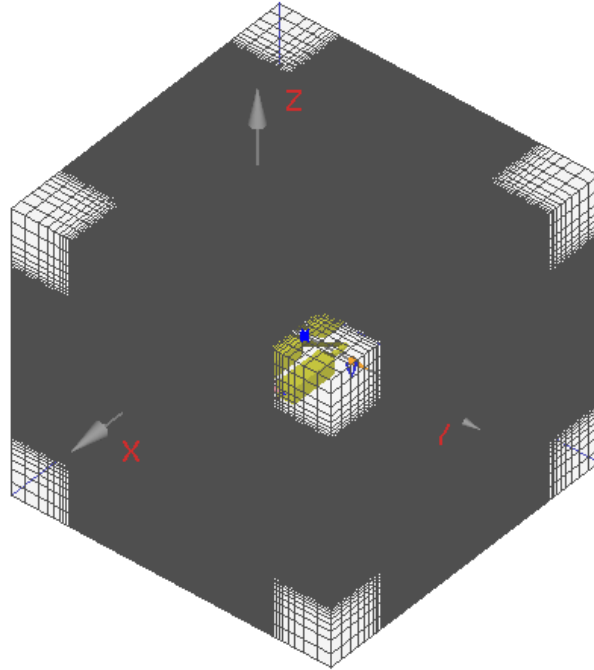


Fig. 5.8: The Cartesian FDTD mesh requires about 408 x 484 x 408 cells to capture the thin wires.

5.5. Wave propagation in a Room

- **Purpose:** Show the high efficiency of the SETD method for large-scale models as a real application.
- **Model:** The problem is a wireless communication in a room to simulate the wave propagation characteristics of the walls and PEC pipes. All walls are modeled by a dielectric material ($\epsilon_r = 2.4$) and 6 PEC pipes located vertically. An incident plane wave source with 1.2 GHz of maximum frequency is used, thus the maximum problem size will be about 19.4 wavelengths for each direction. The plane wave time function is the first derivative of the Blackman-Harris window function.
- **Result:** The SETD method is 51 times less than FDTD method in memory requirement and 1.28 times faster in CPU time as shown in Table 5.5.

Table 5.5: Cost Comparison between SETD and FDTD

	Number of unknowns (Million)	Memory (GB)	CPU Time
SETD	6.58	0.53	5h 50m
FDTD	1,213	27	7h 27m

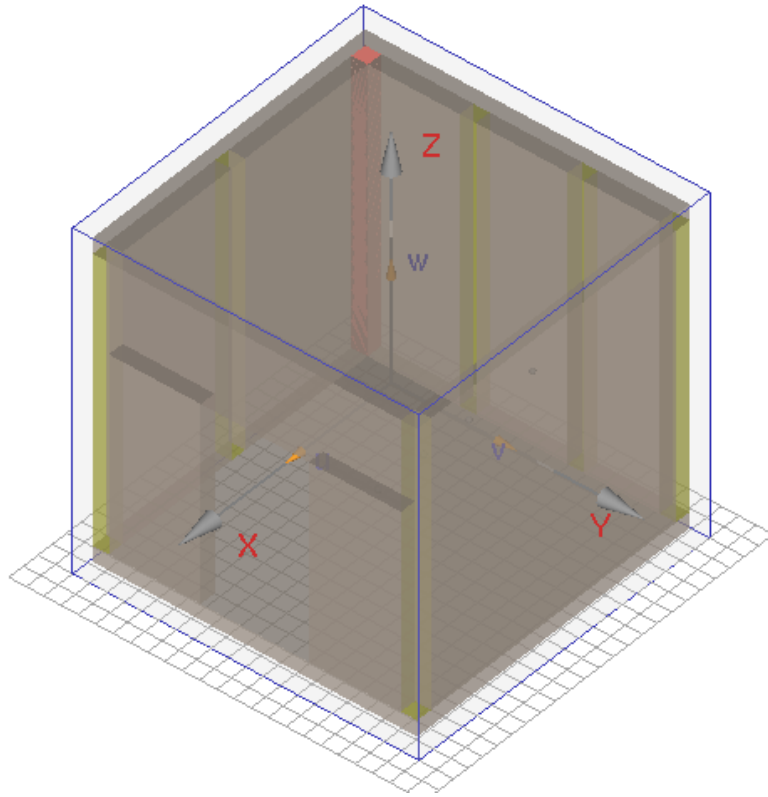


Fig. 5.9: The model of room in a wireless communication setting where all walls are modeled as a dielectric material with PEC pipes located along the z direction. Bounding box of this model is $(-1.6, -1.6, -1.6)$ m (lower corner) to $(1.6, 1.6, 1.6)$ m (upper corner). The plane wave is polarized in the z -direction and propagates along the x -direction. An observer is located at $(-1.2, 0.3, -0.5)$ m to calculate fields.

5.6. A Communication System

- **Purpose:** Show the capability of *Wavenology EM* in simulating a communication system with modulation and demodulation units by the ECT field solver and SPICE circuit solver inside our software.
- **Model:** This system consists of two parts: one is a transmitter using a patch antenna and the other is a receiver using a monopole antenna. The observed electric field at $(0, 250, 20)$ mm, located at the center of the computational domain where we can observe the waveform including both carrier and signal generated at the transmitter.
- **Result:** We confirm that the ECT combined with the nonlinear SPICE solver can model and analyze the communication system very conveniently within one single simulation. Other similar systems with complicated circuits can be also analyzed by our software.

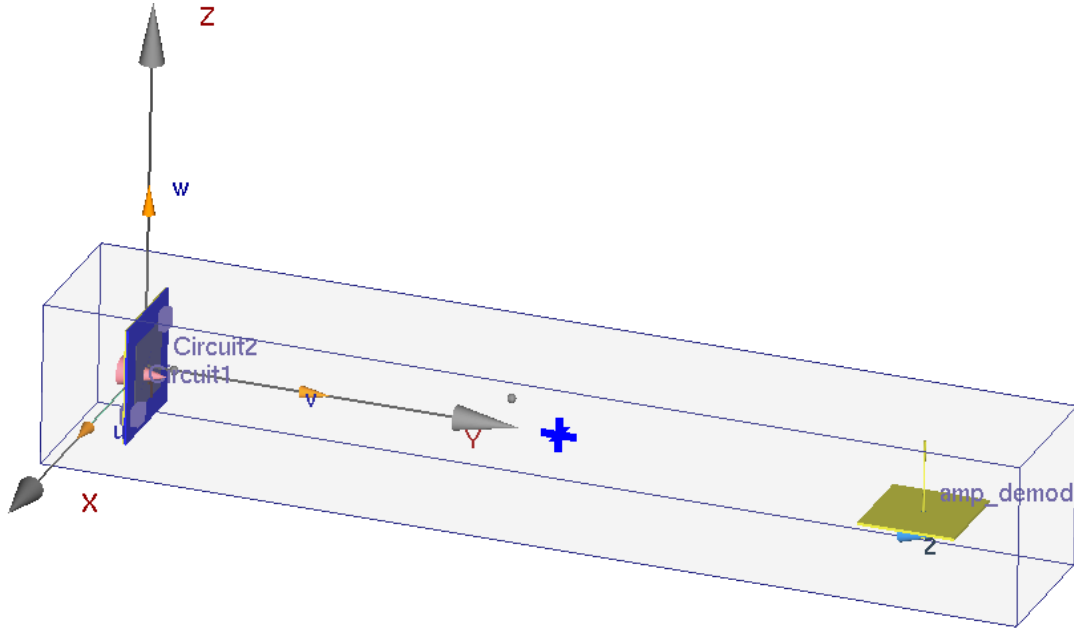


Fig. 5.10: Model of the communication system including transmitter (left) and receiver (right). The substrate in the transmitter has a dimension of 76 mm x 1.5875 mm x 79.5 mm and a dielectric constant of 4.24. The receiver is located about 500 mm away from the transmitter.

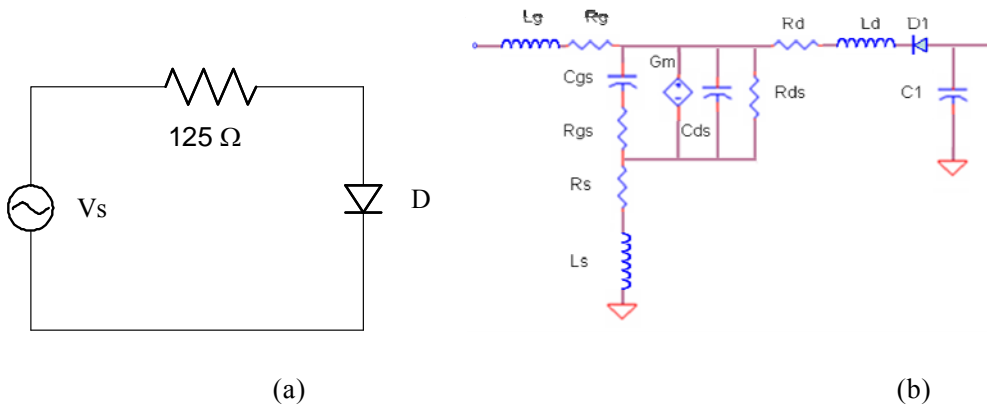


Fig. 5.11: SPICE circuits in the communication system in Fig. 5.10. (a) Modulation circuit denoted as Circuit1 and Circuit2 in the transmitter in Fig. 5.10. (b) Demodulation circuit denoted as “amp_demod” in the receiver in Fig. 5.10.

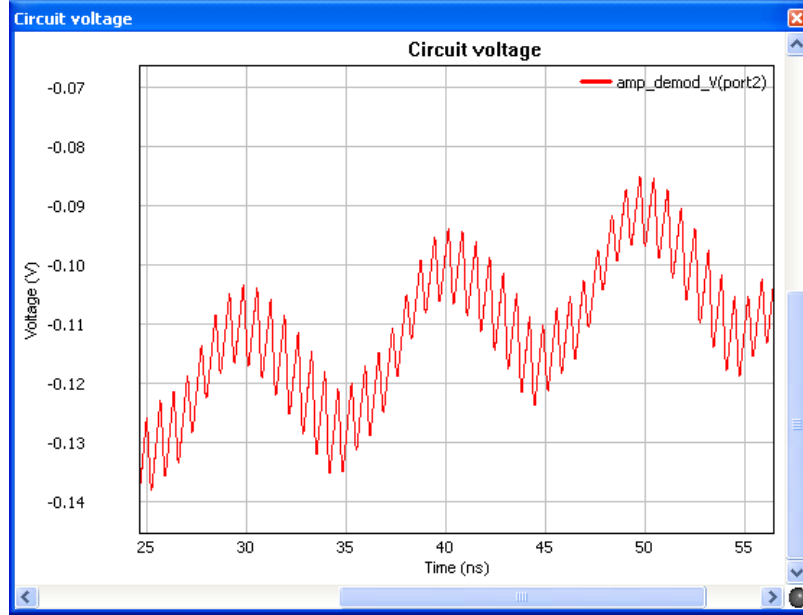


Fig. 5.12: Demodulated signal filtered by the demodulator in the receiver in Fig. 5.10.

5.7. A Patch Antenna Modulated by Dual Memristors

- **Purpose:** Model the directly modulated microstrip patch antenna system with dual memristors [1] by our ECT with the nonlinear SPICE solver.
- **Model:** An L-band directly modulated microstrip patch antenna is chosen. The dielectric constant of the substrate is 4.24 and relative permeability is 1. The area of the square patch is $47.5 \times 47.5 \text{ mm}^2$, approximately equally to half-wavelength in the dielectrics. The feeding point is located at (24.3, 24.3) mm, approximately quarter-wavelength in the dielectrics, on the top patch plane.
- **Result:** The memristive system using a directly modulated patch antenna system with dual memristors has been analyzed successfully by our ECT within Wavenology EM with the nonlinear SPICE solver. We can expect that this method is also applicable to a variety of mechanisms underlying the direct modulation effects.

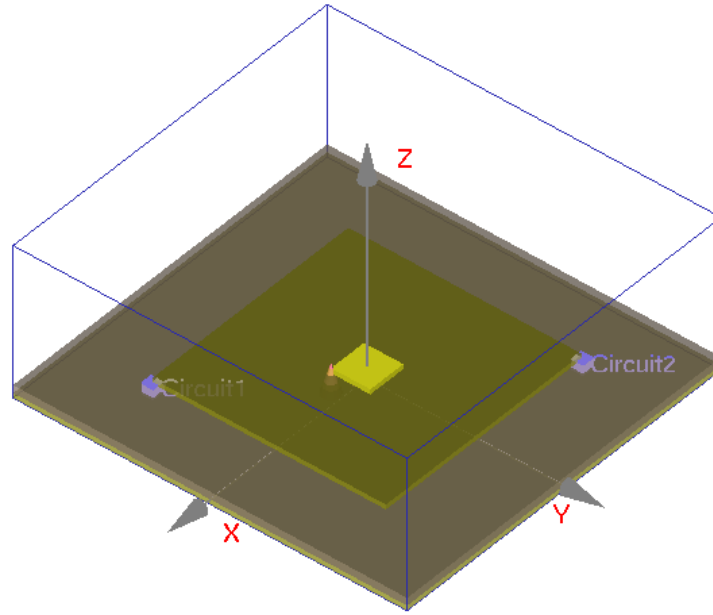


Fig. 5.13: Dual memristors embedded in an L-band directly modulated patch antenna. Circuit1 and Circuit2 denote the memristors.

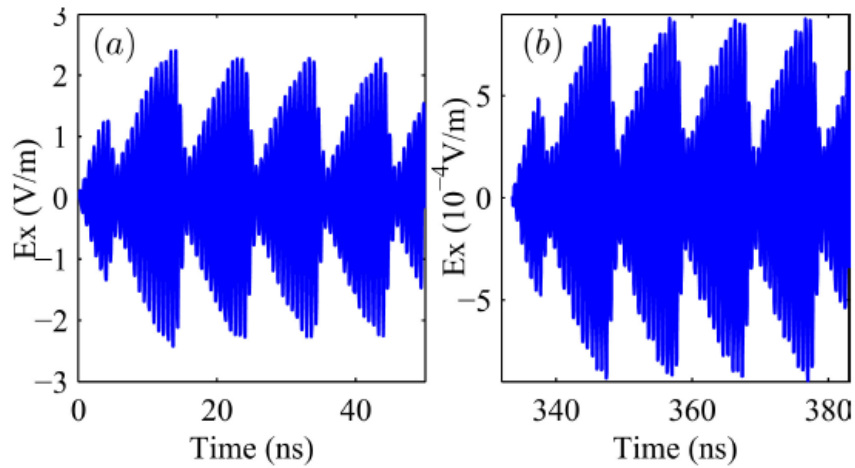


Fig. 5.14: Radiated field by the memresistor modulated patch antenna in Fig. 5.13. (a) Calculated near electric field E_x at (0, 20, 0) mm. This field is a combined nonlinear response of a 1.455 GHz sinusoidal carrier wave and a 100 MHz baseband signal. (b) Calculated far field E_x at (0, 0, 200) mm.

5.8. Antenna Array

- **Purpose:** Show the capability of Wavenology EM in modeling complicated structures including antenna arrays.
- **Model:** The considered patch antenna array is fabricated on an imaging chamber. The structure

of patch antenna array introduces an inhomogeneous background medium. The substrate is FR4 whose ϵ_r is equal to 4.9 and its thickness is 1.6 mm. The medium beyond the patch is a matching medium, acetone. There are eight interlacing antennas on each side panel. All the eight antennas share a ground. The four side walls are fabricated with identical antenna array, totally 32 antennas. The bottom is sealed by a single layer copper PCB board, while the top is open. The chamber is filled with acetone, the matching medium to image biological tissue such as the female breast.

- **Result:** The example shows that the FDTD method can deal complicated model and can be used in many applications such as an inverse problem solver.

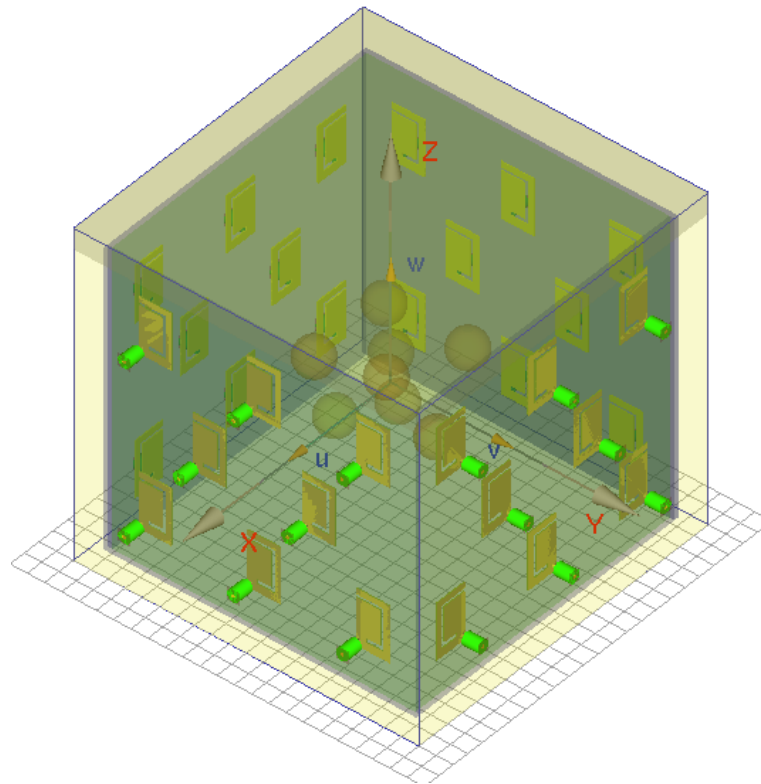


Fig. 5.15: Numerical model of the patch antenna and chamber. 12 x 12 x 12 of observers are located inside the chamber with 4 mm distance from each other; 32 waveports at the feeds of the antennas on four side walls are used as sources to excite the fields sequentially. Dielectric spheres are target objects to be reconstructed in an inverse problem solver.

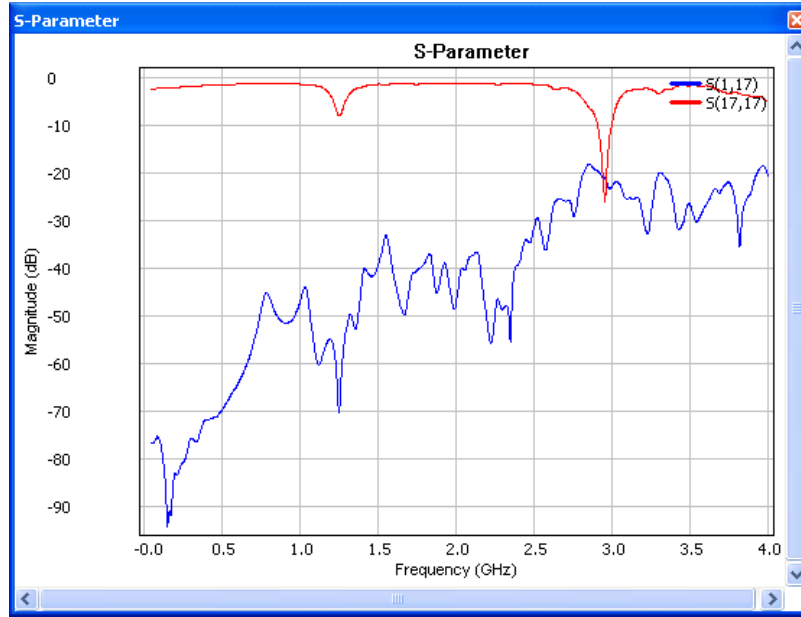


Fig. 5.16: S-Parameters of the patch antenna and chamber when port 17 is used as the source.

5.9. Dual-Band Printed Electrically Small Antenna

- Purpose:** This model provides a dual-band compact ESA unit suitable for the MIMO application in smart and portable wireless devices.
- Model:** Fig. 5.17 presents the configuration of the dual-band electrically small antenna with two capacitive split-ring resonators (SRR). This ESA structure is fed by a high performance 50 Ω coaxial RF sub-Miniature version B connector. The inner conductor of this connector is connected to the right strip of the loop and the outer pins of the connector are directly soldered to the left strip of the loop. The ESA operates at dual frequency bands. The fundamental idea is that two resonant modes are achieved through the field interaction among SRRs and the small loop. In this interaction, two capacitive SRRs play the role of impedance matching to the small loop.
- Result:** Fig. 5.18 shows the measured and simulated return loss of the antenna where we can see that the simulated result has a good agreement with the measured one. The resonant frequencies are about 934 MHz and 1.55 GHz. The bandwidth at the lower band is about 3.76% at -8 dB level and the bandwidth at the higher band is around 2.58%. Both bandwidths, lower than the bandwidth of a conventional loop antenna, are subjected to the large Q-factor from the strong self-resonance of SRRs.

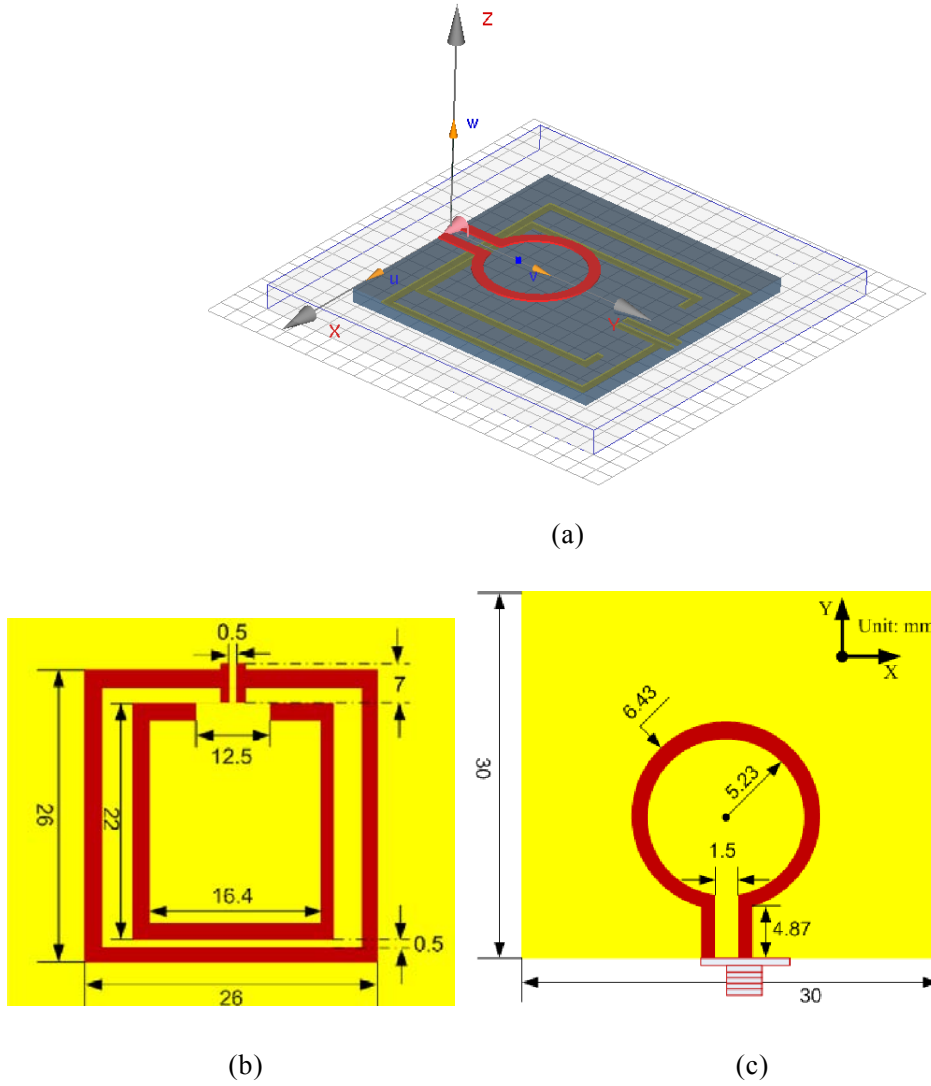


Fig. 5.17: The ESA configuration. (a) Perspective view. (b) Geometry of the SRRs on the bottom. (c) Geometry of the loop on the top.

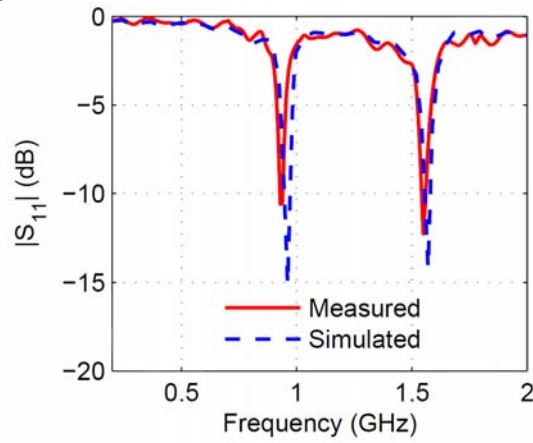


Fig. 5.18: $|S_{11}|$ comparison between measurement and simulation, which shows the operating frequencies are 934 MHz and 1.55 GHz.

5.10. Simple Multiple-Channel Communication

- **Purpose:** Test multiple-channel communication with modulation and demodulation units by the ECT field solver and SPICE circuit solver inside our software. We have tested a single-channel communication at 5.6 A Communication System where the medium is homogeneous. And this model will be an extended version of the previous case.
- **Model:** Fig. 5.19 shows the model which consists of soil on bottom and walls on the other sides. The configuration is similar to the previous case. The transmitter includes a lumped port with a carrier at frequency 1.455 GHz and also modulators, denoted as Circuit1 and Circuit2, which generate a CW signal with 0.1 GHz frequency.
- **Result:** Demodulated signal filtered by the demodulator in the receiver is shown in Fig. 5.20 (a) and that by the previous case is as also shown in Fig. 5.20 (b) for comparison. From these figures we can observe that the magnitude of demodulated signal is less than that of the previous case, because this model has multiple channels due to multiple reflections.

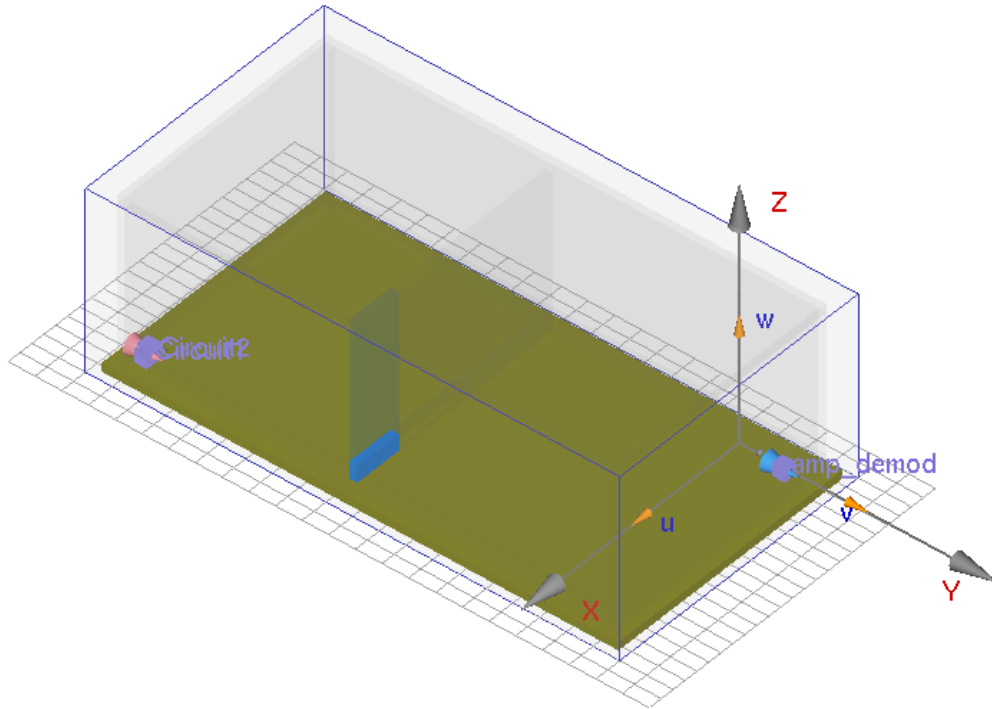
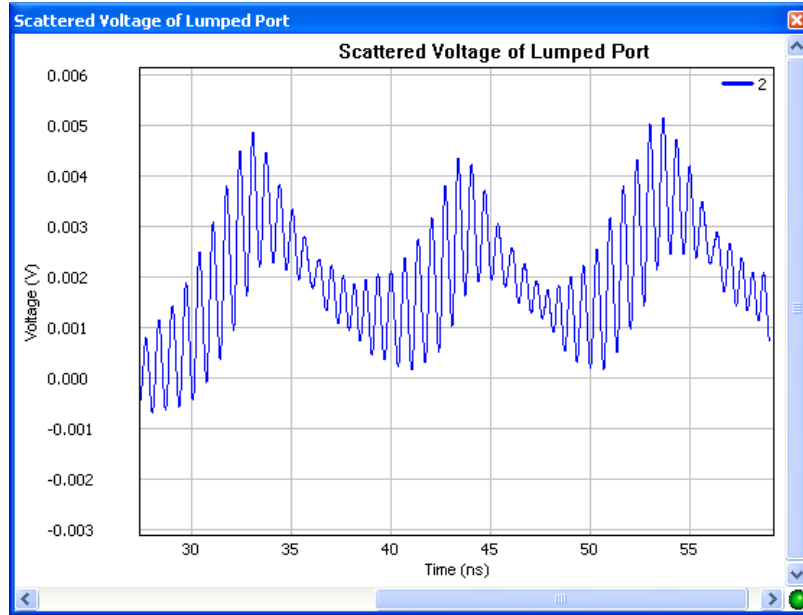
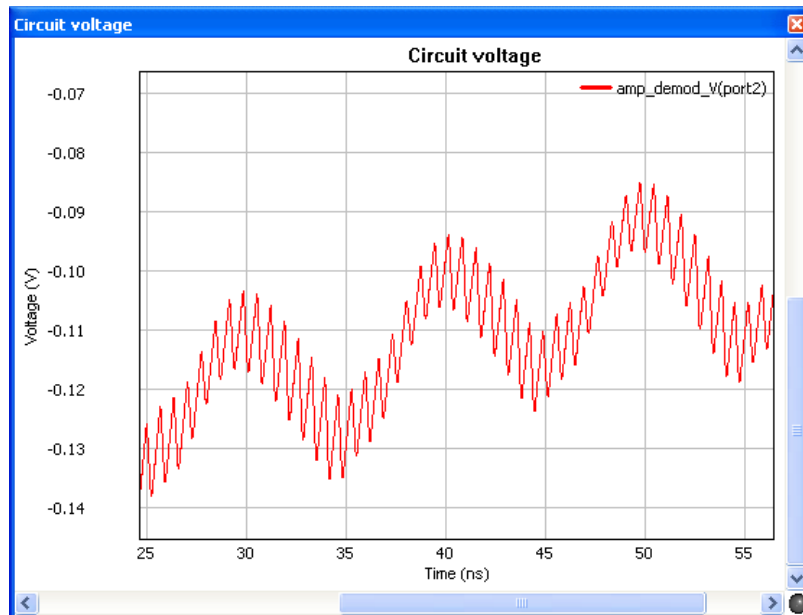


Fig. 5.19: Simple multiple-channel communication room which has a dimension of 3.2 m x 6.2 m x 2.0 m.



(a)



(b)

Fig. 5.20: Demodulated signal filtered by the demodulator in the receiver, (a) from this model, and (b) from the last model (5.6 A Communication System).

5.11. Complicated Multiple-Channel Communication

- **Purpose:** Show a complicated multiple-channel communication system which is more realistic

version of the last model.

- **Model:** This example has many furniture and many electronic devices which can be modeled by wood and PEC, respectively as shown in Fig. 5.21. The other configurations are the same as the last model. Due to complicate objects including wall and soil traveling signal can be reflected and decay.
- **Result:** Fig 5.22 shows demodulated signals filtered by the demodulator from this model and the last model. We can observe that the magnitude of this signal is less than that of the last model. The reason is that the reflection by objects in the model is larger than that in the last model and it causes more decay. As seen in the above results, we confirm that *Wavenology EM* combined with the nonlinear SPICE solver can analyze or design complicated multiple-channel communication systems.

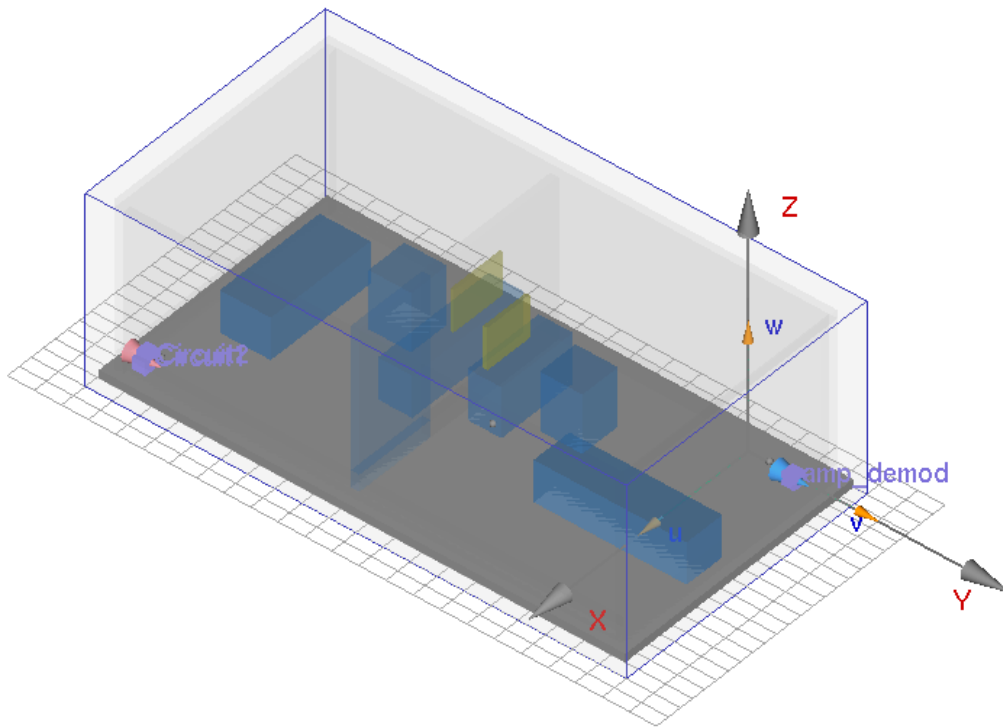


Fig. 5.21: Complicated multiple-channel communication room which has a dimensions of 3.2 m x 6.2 m x 2.0 m.

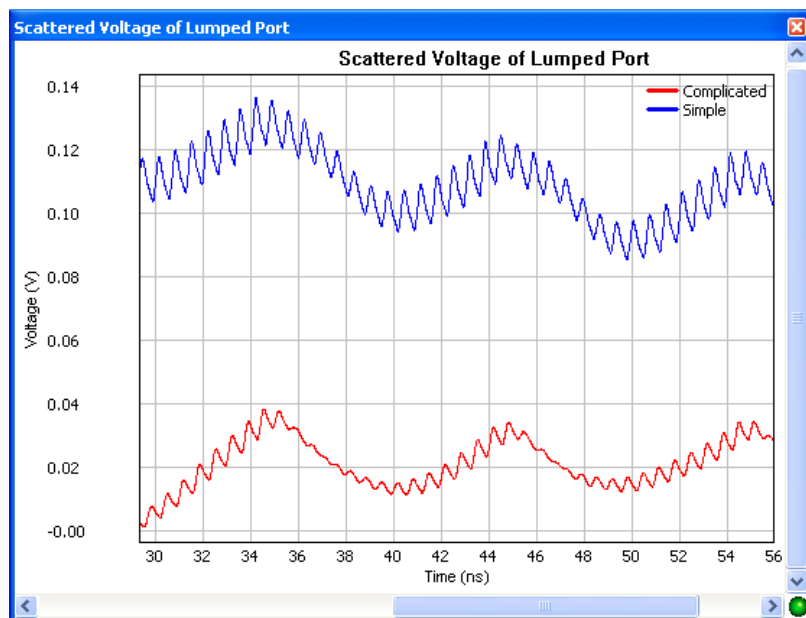


Fig. 5.22: Demodulated signal filtered by the demodulator in the receiver in Fig. 5.21.

6. CONCLUSION

We have developed a new multiscale field/circuit solver by combining three efficient methods: the SETD method, FETD method and ECT method. We have prepared a detailed requirement analysis of a software tool for field/circuit applications from the view of point of the users. And then we have designed an architecture for our software, especially a simple multidomain structure to support several different methods and their coupling required by the multiscale hybrid algorithm. Based on the architecture we have completed the development of the multi-domain ECT engine for field/circuit simulation for a potential better performance under parallel computation and a preparation for our hybrid method. Finally we have completed the development of the hybrid SETD/FETD/ECT/Circuit engine for multiscale simulation. Employing the fact those multidomain methods are well suited to parallel computation, we have completed the parallel computation for our hybrid method based on multi-scale field/circuit package. And we also have completed the implementation of hardware (GPU) acceleration method for the package.

To verify our package, we have completed comprehensive tests of the field/circuit package. The test cases include: (a) A plane wave incident on a large domain to examine the performance of the DG-SETD method; (b) Scattering of a tilted thin PEC plate to an electric dipole wave to examine the performance of hybrid FETD/FDTD method; (c) A patch antenna in a reverberation chamber to examine the performance of the hybrid FETD/SETD method; (d) A tilted parallel wire transmission line connected lumped ports to examine the integration of the hybrid method with circuit elements. (e) Wave propagation in a room as a realistic large domain to examine the performance of the SETD method and compare its result with the FDTD result; (f) Communication system to show a capability of modeling with a communication system with modulation and demodulation by FDTD with SPICE, from the beginning to the end; (g) A patch antenna modulated by dual memristors, which is the first such system to be analyzed by a combined field-circuit solver, where transient electromagnetic radiation is modulated by a nonlinear memristive system, to show the capability of the FDTD field solver with the SPICE circuit solver; (h) A complicated 3D antenna array for microwave imaging; it has complicated structures, numerous observers, and multiple wave ports, to show the usefulness and flexibility of Wavenology EM solver. (i) A dual-band printed electrically small antenna which is fundamentally important for modern wireless communication systems; (j) A simple multiple-channel communication using the ECT field solver and SPICE circuit solver inside our software; (k) A complicated multiple-channel communication which shows *Wavenology EM* combined with the nonlinear SPICE solver can analyze or design complicated multiple-channel communication systems.

REFERENCE

- [1] K. Fujimori, N. Kawashima, M. Sanagi, and S. Nogi, "An efficient LE-FDTD method for the analysis of the active integrated circuit and antenna mounted non-linear devices," *IEICE Transactions on Electronics*, v.E90C, n.9, p.1776-1783, September 2007.
- [2] C. Railton, and J. Schneider, "An Analytical and Numerical Analysis of Several Locally Conformal FDTD Schemes," *IEEE Trans. on Microwave Theory and Tech.*, Vol. 47, pp. 51-66, 1999.
- [3] K. H. Dridi, J. S. Hesthaven and A. Ditkowski, "Staircase free finite-difference time-domain formulation for general materials in complex geometries," *IEEE Trans. Antennas Propagat.*, vol. 49, no. 5, May 2001.
- [4] W. Sui, D. A. Christensen and C. H. Durney, "Extending the two-dimensional FD-TD method to hybrid electromagnetic systems with active and passive lumped elements," *IEEE Trans. Microwave Theory Tech.*, vol. 40, pp. 724–730, Apr. 1992.
- [5] M. Piket-May, A. Taflove, and J. Baron, "FD-TD modeling of digital signal propagation in 3-D circuits with passive and active loads," *IEEE Trans. Microwave Theory Tech.*, vol. 42, pp. 1514–1523, Aug. 1994. (3-D FDTD method is proposed with lumped circuit elements.)
- [6] V. A. Thomas, M. E. Jones, M. Piket-May, A. Taflove, and E. Harrigan, "The use of SPICE lumped circuits as sub-grid models for FDTD analysis," *IEEE Microwave Guided Wave Lett.*, vol. 4, pp. 141–143, May 1994.
- [7] P. Ciampolini, P. Mezzanotte, L. Roselli, and R. Sorrentino, "Accurate and efficient circuit simulation with lumped-element FDTD technique," *IEEE Trans. Microwave Theory Tech.*, vol. 44, pp. 2207–2215, Dec. 1996.
- [8] C.-N. Kuo, R.-B. Wu, B. Houshmand, and T. Itoh, "Modeling of microwave active devices using the FDTD analysis based on the voltage source approach," *IEEE Microwave Guided Wave Lett.*, vol. 6, pp. 199–201, May 1996.
- [9] C. Kuo, B. Houshmand, and T. Itoh, "Full-wave analysis of packaged microwave circuits with active and nonlinear devices: An FDTD approach," *IEEE Trans. Microwave Theory Tech.*, vol. 45, pp. 819–826, May 1997.
- [10] K. Guillouard, M. F. Wong, V. F. Hanna, and J. Citerne, "A new global time-domain electromagnetic simulator of microwave circuits including lumped elements based on finite-element method," *IEEE Trans. Microwave Theory Tech.*, vol. 47, pp. 2045–2049, Oct. 1999.
- [11] S. Chang, R. Coccioli, Y. Qian, and T. Itoh, "A global finite-element time-domain analysis of active nonlinear microwave circuits," *IEEE Trans. Microwave Theory Tech.*, vol. 47, pp. 2410–2416, Dec. 1999.

- [12] H.-P. Tsai, Y. Wang, and T. Itoh, "An unconditionally stable extended (USE) finite-element time-domain solution of active nonlinear microwave circuits using perfectly matched layers," *IEEE Trans. Microwave Theory Tech.*, vol. 50, pp. 2226–2232, Oct. 2002.
- [13] C. Yang and V. Jandhyala, "A time domain surface integral technique for mixed electromagnetic and circuit simulation," Univ. Washington, Seattle, WA, UWEE Tech. Rep. UWEETR-2003-0001, 2003.
- [14] K. Aygun, B. C. Fischer, J. Meng, B. Shanker, E. Michielssen, "A fast hybrid field-circuit simulator for transient analysis of microwave circuits," *IEEE Trans. Microwave Theory Tech.*, vol. 52, no. 2, pp. 573-583, Feb. 2004.
- [15] L.W. Nagel, "SPICE2: A computer program to simulate semiconductor circuits," Univ. California, Berkeley, CA, Memo UCB/ERL M75/520, 1975. [SPICE2 original reference]
- [16] A. Vladimirescu, *The SPICE Book*. New York: Wiley, 1994. [SPICE reference]
- [17] T. Xiao, and Q. H. Liu, "Enlarged cells for the conformal FDTD method to avoid the time step reduction," *IEEE Microwave Wireless Compon. Lett.*, vol. 14, pp. 551-553, 2004.
- [18] S. Gedney, and F. Lansing, "Explicit Time-Domain Solutions of Maxwell's Equations Using Non-Orthogonal and Unstructured Grids," in *Computational Electrodynamics: The Finite Difference Time Domain Method*, A. Taflove, Ed., Artech House, Boston, MA, 1995.
- [19] S. Dey and R. Mittra, "A locally conformal finite-difference time-domain (FDTD) algorithm for modeling three-dimensional perfectly conducting objects," *IEEE Microwave Guided Wave Lett.*, vol. 7, pp. 273-275, Sept. 1997.
- [20] T. Xiao, and Q. H. Liu, "A staggered upwind embedded boundary method to eliminate the FDTD staircasing error," *IEEE Trans. Antennas Propagat.*, vol. 52, no. 3, pp. 730-741, March 2004.
- [21] B. Yang, D. Gottlieb, J. S. Hesthaven, "Spectral simulation of electromagnetic wave scattering," *Journal of Computational Physics*, vol. 134, no. 2, pp. 216-230, 1997.
- [22] J. S. Hesthaven, "Spectral collocation time-domain modeling of diffractive optical elements," *Journal of Computational Physics*, vol. 155, no. 2, pp. 287-306, 1999.
- [23] Q. H. Liu, and G. Zhao, "Review of PSTD methods for transient electromagnetics," *International Journal of Numerical Modeling: Electronic Networks, Devices and Fields*, vol. 22, no. 17, pp. 299-323, 2004.
- [24] Q. H. Liu, and G. Zhao, "Advances in PSTD Techniques," Chapter 17, *Computational Electromagnetics: The Finite-Difference Time-Domain Method*, A. Taflove, and S. Hagness, Ed., Artech House, Inc., 2005.
- [25] G. Zhao, and Q. H. Liu, "The 2.5-D multidomain pseudospectral time-domain algorithm," *IEEE Trans. Antennas Propagat.*, vol. 51, no. 3, pp. 619-627, March 2003.

- [26] G. Zhao, Y. Q. Zeng, and Q. H. Liu, "The 3-D multidomain pseudospectral time-domain method for wideband simulation," *IEEE Microwave Wireless Compon. Lett.*, vol. 13, no. 5, pp. 184-186, 2003.
- [27] G. Zhao, and Q. H. Liu, "The unconditionally stable multidomain pseudospectral time-domain method," *IEEE Microwave Wireless Compon. Lett.*, vol. 13, no. 11, pp. 475-477, 2003.
- [28] G. Zhao, and Q. H. Liu, "The 3-D multidomain pseudospectral time-domain method for inhomogeneous conductive media," *IEEE Trans. Antennas Propagat.*, vol. 52, no. 3, pp. 742-749, March 2004.
- [29] T. Xiao, and Q. H. Liu, "A 3-D enlarged cell (ECT) technique for the conformal FDTD method," *IEEE Trans. Antennas Propagat.*, vol. 56, no. 3, pp. 765-773, March, 2008.
- [30] T. Xiao, and Q. H. Liu, "Three-dimensional unstructured-grid discontinuous Galerkin method for Maxwell's equations with well-posed perfectly matched layer," *Microwave Opt. Technol. Lett.*, vol. 46, no. 5, pp. 459-463, 2005.
- [31] J.-H. Lee, and Q. H. Liu, "A 3-D spectral element time-domain method for electromagnetic simulation," *IEEE Trans. Microwave Theory Tech.*, vol. 55, no. 5, pp. 983-991, May 2007.
- [32] J.-H. Lee, J. Chen, and Q. H. Liu, "A 3-D discontinuous spectral element time-domain method for Maxwell's equations," *IEEE Trans. Antennas Propagat.*, vol. 57, no. 9, pp. 2666-2674, Sep 2007.
- [33] C.-C. Wang and C.-W. Kuo, "An efficient scheme for processing arbitrary lumped multiport devices in the finite-difference time-domain method," *IEEE Trans. Microw. Theory Tech.*, vol. 55, no. 5, pp. 958-965, May 2007.
- [34] W. Yao and Y. Wang, "Direct antenna modulation – a promise for ultra-wideband (UWB) transmitting", *Microwave Symposium Digest, 2004 IEEE MTT-S International*, July 2004.
- [35] S. Keller, *Design and Development of Directly-Modulated Antennas Using High-Speed Switching Devices*, Ph.D. Dissertation, Duke University, 2008.
- [36] S. D. Keller, W. D. Palmer, W. T. Joines, "Direct modulation of an L-band microstrip patch antenna using integrated PIN diodes", *Allerton Antenna Applications Symposium*, Monticello, IL, September 2006.
- [37] S. D. Keller, W. D. Palmer, W. T. Joines, " Electromagnetic modeling and simulation of a directly-modulated L-band microstrip patch antenna", *IEEE Antennas and Propagation Society International Symposium*, Honolulu, HI, June 13, 2007.
- [38] B. Zhu, J. Chen, W. Zhong, and Q. H. Liu, "A hybrid FETD-FDTD method with nonconforming meshes," *Commun. Comput. Phys.*, vol. 9, no. 3, pp. 828-842, 2011. doi: 10.4208/cicp.230909.140410s.